Chemical Engineering Journal 541 (2026) 177731

Contents lists available at ScienceDirect

Chemical Engineering Journal

journal homepage: www.elsevier.com/locate/cej

Application of a three-phase fluidized bed electrode for an electro-enzymatic batch process with the peroxygenase *Aae*UPO

Michael Abt [a], Carolin Kienzle [a], Melissa Ditzel [a], Mirco Jestädt [a], Katharina Bleher [a], Matthias Franzreb [a], André Tschöpe [a,*]

[a] Institute of Functional Interfaces, Karlsruhe Institute of Technology, Hermann-von-Helmholtz-Platz 1, 76344, Eggenstein-Leopoldshafen, Germany

ARTICLE INFO

Keywords:
Electro-enzymatic
Fluidized bed electrode
Unspecific peroxygenase (*Aae*UPO)
In-situ H_2O_2
Hydroxylation

ABSTRACT

Electrification of biological syntheses offers a sustainable route to decarbonize chemical production. This requires innovative reactor concepts that combine efficient electrochemical reaction steps with selective biocatalysts. Unspecific peroxygenases (UPOs) are attractive because they hydroxylate non-activated C—H bonds and need only hydrogen peroxide (H_2O_2) as co-substrate. However, excess H_2O_2 rapidly deactivates UPOs. Electrochemical reactors must therefore generate H_2O_2 in-situ at low, uniform levels while maintaining strong mixing and mass transfer — a capability conventional electrochemical cells struggle to provide. Here, we present the first three-phase electrochemical fluidized bed reactor (gas–liquid–solid) for combined electro-enzymatic synthesis. This reactor utilizes conductive graphite particles as a fluidized electrode on which oxygen reduction generates H_2O_2 throughout the particle bed, while air sparging resupplies O_2 and drives mixing, enhancing mass transfer. Using the unspecific peroxygenase from *Agrocybe aegerita* (*Aae*UPO) as a model enzyme, we successfully optimized the electrochemical H_2O_2 generation rate to maintain non-inhibitory H_2O_2 concentrations below 0.2 mM and achieved a high current efficiency of 54.5 ± 12.5% for enzymatic product formation. Moreover, the batch process demonstrated scalability, as increasing the enzyme concentration enabled a $Y_{HEBA/EBA}$ of ~100% at even higher H_2O_2 generation rates, resulting in a space-time yield (STY) of 38.83 ± 0.32 g/(L·d) for the hydroxylation of 4-ethylbenzoic acid (EBA) to 4-(1-hydroxyethyl)benzoic acid (HEBA). These results establish the electrochemical fluidized bed reactor as a highly efficient platform for electro-enzymatic synthesis, particularly for processes requiring in-situ co-substrate generation.

1. Introduction

The chemical and pharmaceutical industries increasingly rely on biocatalysis for highly specific active compounds to address complex scientific and therapeutic challenges [1–5]. However, traditional chemical synthesis often struggles to produce these structurally sophisticated molecules cost-effectively, as each target typically requires multiple reaction and purification steps [6]. In contrast, enzymatic syntheses offer an efficient alternative, enabling highly selective and direct catalysis with fewer reaction steps [6,7]. Despite these advantages, applying biocatalysts at an industrial scale faces two central hurdles: (1) limited enzyme stability [6,8,9] and (2) the frequent requirement for costly co-factors (e.g. NAD^+/NADH and ATP) [10–13]. One possibility for overcoming the aforementioned challenges is the field of electrobiotechnology. By combining electrochemistry and biotechnology, cost-intensive co-factors can be replaced, supplied, or regenerated [14–17]. However, pure electrochemical regeneration for instance of NAD^+/NADH is often limited by poor selectivity, yielding inactive isomers and dimers. Therefore, recent approaches employ artificial mediators (e.g. viologen derivatives) to enhance electron transfer and partially replace nicotinamide cofactors. In general, electron transfer in such systems can occur either directly between electrode and enzyme or indirectly via mediators, redox polymers, or further enzymes (e.g. diaphorases). [18–22]

Oxidoreductases are an important class of enzymes already used in electro-enzymatic processes, where many catalyze reactions involving nicotinamide cofactors such as NAD^+/NADH, enabling specific functionalizations that are difficult to achieve by conventional chemical syntheses. Within this class, unspecific peroxygenases (UPOs), first reported from the fungus *Agrocybe aegerita* [23], have emerged as

* Corresponding author.
E-mail address: andre.tschoepe@kit.edu (A. Tschöpe).

https://doi.org/10.1016/j.cej.2026.177731
Received 13 February 2026; Received in revised form 5 May 2026; Accepted 25 May 2026
Available online 1 June 2026

promising candidates, as they are able to catalyze various reactions, including the hydroxylation of non-activated C—H bonds while requiring only H_2O_2 as co-substrate, thereby avoiding the need for nicotinamide cofactors. [24–27] However, UPOs are highly sensitive to the co-substrate hydrogen peroxide, which poses a significant challenge and can lead to enzyme inactivation. Thus, excessive hydrogen peroxide inhibits the enzyme, necessitating novel reactor designs that can supply precise and controlled amounts of this co-substrate in-situ [28–30].

So far, a range of electrochemical strategies has been explored to enable on-demand hydrogen peroxide generation, including gas-diffusion electrodes [17,31–34] and integrated all-in-one electrode systems [30,35]. These methods share certain key requirements for electro-enzymatic processes such as near-neutral pH, low electrolyte concentration, and sufficiently large electrode surfaces that provide adequate current density [19,32,36,37]. At the same time, this on-demand electrochemical generation of hydrogen peroxide circumvents the volume increase associated with bulk H_2O_2 dosing [29], thereby preserving enzyme performance and enabling high total turnover numbers (TTNs) and space-time yields (STYs) [17,38–40]. However, a major disadvantage of these investigated electrode strategies is that hydrogen peroxide is produced locally at a specific surface within the reactor volume, which may lead to concentration gradients rather than volumetric distribution. As a result, scaling production involves adding multiple electrodes [41,42] and requires electrochemically often stacked electrode assemblies [43] (numbering-up) rather than simple volumetric scale-up.

One type of electrode that enables volumetric scaling is the so-called particle electrode, which consists of a bed or packing of conductive electrode particles [44–50]. Such particle electrodes also fulfil conditions advantageous for electro-enzymatic processes, including a low current density and a large electrode surface [51]. In this context, particle electrodes can be divided into fixed bed electrodes and fluidized bed electrodes [36,52], the latter showing beneficial characteristics in terms of the avoidance of gas retention during electrochemical operation. If the electrochemical reaction system contains a gas phase, the gas bubbles can pass through the fluidized, reducing bubble retention within the particle bed and minimizing blockage of the electrode surface area [51]. In addition, fluidized beds typically offer enhanced mass transfer properties compared to fixed beds [36]. As far as we know, however, fluidized bed electrodes have never been used in electro-enzymatic processes. Fields of application for particle electrodes in electro-enzymatic processes are more likely to be found in the use of fixed bed electrodes. For instance, two-phase fixed-bed electrode configurations have been applied to generate the co-substrate hydrogen peroxide via reduction of pre-dissolved oxygen [53] and to regenerate nicotinamide co-factors, either NADH through mediator-assisted reduction [54] or NAD^+ through mediator-assisted oxidation [55]. In contrast, fluidized bed electrodes find a wider range of applications in electrobiotechnology in electro-microbial processes [36], especially in the treatment of wastewater with electroactive microorganisms [56–58]. In a previous publication, we developed a novel three-phase fluidized bed reactor, a specific type of particle electrode reactor, for the electrochemical co-substrate generation of hydrogen peroxide under enzyme compatible conditions [51]. This reactor features a fluidized bed of inexpensive, conductive graphite particles, forming a three-dimensional particle electrode. The design demonstrated the feasibility of effectively producing hydrogen peroxide in-situ in both batch and continuous operation by reducing dissolved oxygen to H_2O_2. Due to the low solubility of oxygen, air sparging was introduced to redeliver consumed oxygen, and to fluidize the particle electrode. This brings the advantage of a well-mixed reactor and enhanced mass-transfer [51].

In this work we investigate for the first time the coupled in-situ generation of hydrogen peroxide and enzymatic reaction in this novel three-phase fluidized bed reactor. Thereby, the enzymatic reaction is represented by the model reaction from 4-ethylbenzoic acid (EBA) to 4-(1-hydroxyethyl)benzoic acid (HEBA) catalyzed by the unspecific peroxygenase from *Agrocybe aegerita* (*Aae*UPO). We demonstrate the successful operation in a batch process by optimizing the electrochemical H_2O_2 generation and the stability of the enzyme, underscoring the potential of this innovative reactor configuration as a flexible, scalable platform for electro-enzymatic synthesis.

2. Material and methods

2.1. Chemicals

All chemicals used were of analytical grade and applied without further purification. Ultrapure water was obtained from a water purification system (Merck Millipore, USA) and used for preparing all reaction solutions.

2.2. Enzyme

The recombinant, unspecific peroxygenase r*Aae*UPO (referred to in many studies as PaDa-I mutant), a variant originally developed by the research group of Miquel Alcalde [59,60], was supplied from the research group of Frank Hollmann. The enzyme was produced in a pilot-scale process of 2500 L using the *Pichia pastoris* expression system. [27,61]

The initial protein concentration m_{Protein} was determined in triplicate using the Bradford assay at a wavelength of 595 nm, with a calibration curve based on bovine serum albumin (BSA). A protein-to-protein variation absorbance coefficient of 0.68 ± 0.26 was used. Additionally, the reported purity of the r*Aae*UPO solution $Y_{\mathrm{rAaeUPO/Protein}}$ (i.e. 85% of the overall protein content) was accounted [61], along with its molar mass M_{AaeUPO} of 51.1 kDa [59,60]. The enzyme concentration of r*Aae*UPO was calculated considering volume V and dilution factor f using Eq. (2.1):

$$c_{\mathrm{rAaeUPO}} = \frac{m_{\mathrm{Protein}}}{V \bullet M_{\mathrm{rAaeUPO}}} \bullet Y_{\mathrm{rAaeUPO/Protein}} \bullet f \tag{2.1}$$

r*Aae*UPO activity was assessed with veratryl alcohol (VA; 3,4-dimethoxybenzyl alcohol) as a model substrate, with assays run in triplicate and appropriate blanks to account for non-enzymatic reactions. The alcohol oxidation of VA to veratraldehyde was measured at a wavelength of 310 nm in 96-well microtiter plates at 25 °C using a microplate reader (Tecan Spark, Switzerland). The reaction was started by adding either H_2O_2 or the enzyme. Initial rates were obtained from the linear change in absorbance dE/dt and converted to apparent VA activity v_{VA} using Eq. (2.2):

$$v_{\mathrm{VA}} = \frac{dE}{dt \bullet \varepsilon_{\mathrm{VA}} \bullet d} \bullet f \tag{2.2}$$

where $\varepsilon_{\mathrm{VA}}$ is the extinction coefficient (9300 1/(M · cm)) and d is the optical path length. The reaction mixture consisted of 70 µL potassium phosphate buffer (pH 6.1), 100 µL of 50 mM VA solution (25 mM final), 10 µL of 40 mM H_2O_2 (2 mM final) and 20 µL enzyme sample. The enzyme activities were reported in U_{VA}/mL (µmol/(min · mL)) as apparent enzyme activity.

2.3. Analytical methods

Hydrogen peroxide, the co-substrate of the enzymatic reaction, was quantified with a Cu(II)–neocuproine photometric test kit (Supelco Spectroquant, Merck), measuring absorbance at 445 nm in microtiter plates with the microplate reader. Prior to analysis, all samples were diluted to maintain H_2O_2 concentrations below 0.18 mM, guided by semiquantitative enzymatic test strips (Supelco MQuant, Merck).

The in the process targeted enzymatic reaction of EBA to HEBA was analyzed quantitatively using high-performance liquid chromatography (HPLC) (Chromaster, Hitachi, Japan) with a diode array detector. A

gradient elution method (see Fig. S6-S8 in SI) was employed, utilizing mobile phase A (0.1% formic acid in water) and mobile phase B (acetonitrile). The solvent gradient profile was as follows: 1 min – 80% (A), 20% (B); 10 min – 20% (A), 80% (B); 12 min – 80% (A), 20% (B). The total run time was 16 min including a 1 min equilibration time between runs, with HEBA eluting at 2.6 min and EBA at 8.3 min. Chromatographic separation was carried out at a column oven temperature of 35 °C, with samples maintained at 10 °C in the autosampler. Samples of 3 µL volume were injected at ~130 bar and at a flow rate of 0.5 mL/min onto a Gemini 3u C18 110 A column (100 × 3 mm). Detection was performed at 237 nm, and quantification of EBA and HEBA concentrations was based on calibration curves spanning a concentration range of 0.0 to 2.0 mM. All samples were diluted accordingly.

2.4. Kinetic investigation of the EBA to HEBA reaction

Beforehand, a kinetic study was conducted to determine the optimal co-substrate and substrate concentration for the enzymatic conversion. Reaction mixtures were prepared in a total volume of 1 mL, containing 10.9 nM r*Aae*UPO, and varying EBA and H_2O_2 concentrations ranging from 0.2 to 20 mM in potassium phosphate buffer of pH 6.1. The linear reaction range was determined for the initial reaction rate within the tested concentration range. Within this linear range, after 60 s of reaction, the enzymatic activity was halted by adding 10 µL of sodium azide to quench the reaction, and samples were collected for further analysis.

2.5. Electrochemical fluidized bed reactor, concept and setup

A three-phase fluidized bed electrode system, introduced in our previous study [51], was employed for this work. Fig. 1 illustrates the cross-section of the fully 3D-printed setup, comprising a working electrode (WE), a counter electrode (CE), and an Ag/AgCl reference electrode (RE, ALS, Japan). The reactor was divided by a cation exchange membrane (FKB-PK 130 µm PEEK-reinforced, Fumatech, Germany) into a central working electrode chamber (15 mm diameter) and a surrounding counter electrode chamber. Hereby, the working electrode consisted of a bed of commercial graphite particles (Desulco 9018, Superior Graphite, USA) sieved to a particle size of 800–1200 µm. These particles were contacted by a four-layer platinized titanium grid current feeder (9 mm spacing between layers) and thoroughly washed with a 50% (*v*/v) ethanol solution and ultrapure water before use. At the surface of the particle electrode and the current feeder, oxygen was electrochemically reduced to hydrogen peroxide, serving as a co-substrate for the enzyme-catalyzed hydroxylation of EBA to HEBA. Meanwhile, water oxidation occurred at the counter electrode which was built from platinized titanium wire, helping to replenish H^+ ions via the membrane in the buffered working electrode chamber. Additionally, the membrane prevented electrolyte solution mixing, thereby maintaining distinct conditions in each chamber and avoiding side reactions at the counter electrode.

To support H_2O_2 generation and enhance mixing, the working-electrode (WE) chamber was oxygenated via a bottom-mounted air sparger (pore size: 2 µm, Mott, USA). Airflow was controlled by a mass-flow controller (FC260, Tylan General, Germany), fluidizing the electrode particles. Excess air was vented from the top of the WE chamber, and dissolved O_2 was continuously monitored with an oxygen sensor (Oxybase, PreSens, Germany). In parallel, the counter-electrode (CE) electrolyte was recirculated through a 1 L reservoir by a peristaltic pump (ISM 832, Ismatec, Switzerland) to remove O_2 bubbles formed during water electrolysis and to minimize pH drift. The potential between the working and reference electrodes was controlled with a Gamry potentiostat (Interface 5000, Gamry Instruments, USA).

2.6. Electro-enzymatic process

During operation of the fluidized bed reactor, the working electrode chamber was filled with 35 mL of 100 mM potassium phosphate buffer at pH 6.1 and sparged with an air flow rate of 73 mL/min (superficial gas velocity ~7 mm/s), with a volumetric mass transfer coefficient k_La of 1.5 1/min determined by the dynamic gassing method as described previously [51], to ensure oxygen supply and maintain near-saturation dissolved oxygen levels in the bulk liquid. This air flow resulted in the

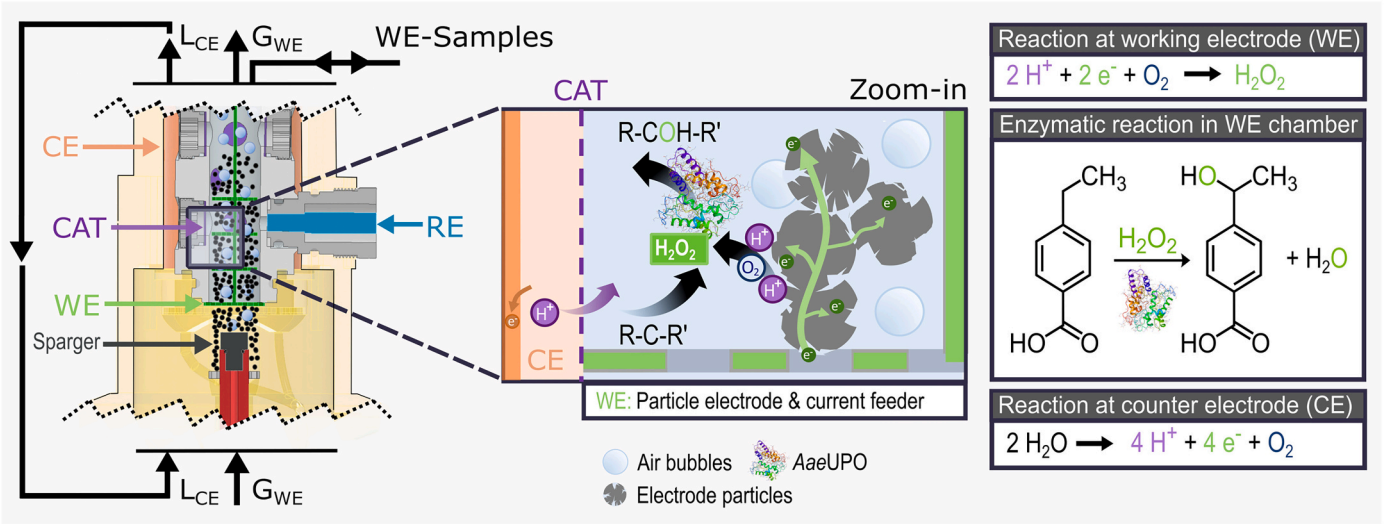

Fig. 1. Graphical representation of the cross-section of the electrochemical fluidized batch reactor of our previous publication [51]. The reactor consisted of two chambers separated by a cation exchange membrane (CAT, purple). The counter (CE, orange) and working electrode (WE, green) were assembled concentrically in a cylindrical reactor shell. The counter electrode was a platinized titanium wire wrapped around the working electrode chamber. The working electrode consisted of graphite electrode particles, that were electrically contacted by a four-level platinized titanium grid. An Ag/AgCl reference electrode (RE, blue) completed the three-electrode setup. In batch operation, the electrode particles were fluidized by air via a gas inlet (G_{WE}, air) and oxygen was resupplied via a sparger rod (red) to the system. The electrolyte in the counter electrode (L_{CE}) was circulated over a reservoir. In the working electrode chamber the enzymatic hydroxylation of EBA to HEBA by unspecific peroxygenase r*Aae*UPO took place. The hydrogen peroxide was generated in-situ at the graphite particle electrode surface by reducing oxygen. All samples were directly taken from the top of the working electrode chamber. At the counter electrode water oxidation occurred, which helped to replenish H^+ ions in the buffered working electrode chamber.

fluidization of 4.5 g graphite electrode particles, occupying an electrode volume of V_e ~7 mL and creating an electrode area of 121.3 cm^2, significantly exceeding the geometric surface area of the four-layer platinized titanium grid current feeder (17.5 cm^2). In parallel, a 250 mM K_2SO_4 solution of pH 3.1 was circulated with 6 mL/min over the counter electrode chamber to maintain stable operation conditions. All samples were taken from the top of the working electrode chamber, and pH was checked periodically.

Before each electro-enzymatic process, we conducted experiments focused on determining the hydrogen peroxide generation rate in the in-situ process. The electrochemical reaction at the particle electrode was initiated by applying a controlled potential via the potentiostat, thereby reducing oxygen to H_2O_2. The potentials −0.40, −0.47, −0.55, and −0.63 V vs. Ag/AgCl were chosen to examine their effect on H_2O_2 production rates. During each experiment, dissolved oxygen levels were monitored, while hydrogen peroxide concentrations were measured at regular intervals.

For the electro-enzymatic process, H_2O_2 production rates were selected based on the preliminary electrochemical investigations, and ~5 mM EBA were initially added in the potassium phosphate buffer of pH 6.1. Furthermore, two different initial enzyme concentrations of 20–24 ± 6 nM and 30–34 ± 9 nM r*Aae*UPO were employed, corresponding approximately to apparent enzyme activities of 0.11–0.13 U_{VA}/mL and 0.19–0.20 U_{VA}/mL. The process was started by applying the respective electrode potential vs Ag/AgCl. Samples were collected in triplicates at regular intervals from the working electrode chamber and replaced with potassium phosphate buffer (~1.7 mL) to maintain volume. For each sample, the apparent enzyme activity, H_2O_2 concentration, the concentrations of EBA and the product HEBA were determined. To quench the enzymatic reaction immediately after sampling for H_2O_2 and EBA/HEBA analysis, 10 µL of sodium azide was added. All analytical measurements were performed using established assays and HPLC methods as previously described.

2.7. Performance and data analysis

The process performance was quantified by production rate $\dot{q}_{p,i}$, space-time yield (STY_i), current density j_a and current efficiency Φ_i^e. For the purely electrochemical reference, these performance indicators were determined for the electrogenerated co-substrate H_2O_2 ($i = H_2O_2$) under identical process conditions to those used for electro-biocatalytic experiments, but without enzyme. Whereas for the combined electro-enzymatic process with enzyme, these performance indicators were calculated with the enzymatic product HEBA (i = HEBA). Unless stated otherwise, these performance indicators were evaluated at 15 min of operation. The total turnover number (TTN_{HEBA}) was calculated over the entire process, from start until no enzyme activity and product formation were detectable. Definitions and calculations for $\dot{q}_{p,i}$, STY_i, j_a, Φ_i^e and TTN_{HEBA} followed our previous studies (see Eqs. S2.1-S2.5 in SI) [51,62].

Furthermore, because repeated withdraw of samples with $V_s = 1.7$ mL was non-negligable in comparison to the reactor volume $V_r = 35$ mL, both product and reactant removal as well as dilution due to buffer refilling were considered within a molar balance of the process (see Eqs. S1.1-S1.5 in SI). To asses all product formed, the total amount including product loss due to sampling was determined. At each sampling point j, the HEBA concentration $c_{HEBA,j}$ in the reactor was used to calculate the lost product amount per sample. The cumulative product loses until the current point of sampling k were then added to the amount of product $V_r \bullet c_{HEBA,k}$ remaining in the reactor. Eq. (2.3) captures the total amount of HEBA $n_{HEBA,total,k}$:

$$n_{HEBA,total,k} = V_r \bullet c_{HEBA,k} + \sum_{j=0}^{k} c_{HEBA,j} \bullet V_s \tag{2.3}$$

Respectively, in Eq. (2.4) the cumulative sampling-induced EBA loss $n_{EBA,samples,k}$ was calculated using the determined EBA concentration $c_{EBA,j}$ from each sample j up to point k:

$$n_{EBA,samples,k} = \sum_{j=0}^{k} c_{EBA,j} \bullet V_s \tag{2.4}$$

To calculate the overall yield $Y_{HEBA/EBA}$ for the entire process, the EBA amount available for conversion $n_{EBA,available}$ was obtained by subtracting the cumulative EBA losses up to the final sample from the initial amount of EBA $n_{EBA,initial} = V_r \bullet c_{EBA,initial}$. The final sample point k_{final} was defined as the time at which no enzyme activity remained (see Eq. (2.5)):

$$n_{EBA,available} = V_r \bullet c_{EBA,initial} - \sum_{j=0}^{k_{final}} c_{EBA,j}(t) \bullet V_s \tag{2.5}$$

The overall yield of the process was then calculated by Eq. (2.6) as the ratio of the final total amount of HEBA (Eq. (2.3)) evaluated at $k = k_{final}$) to the available amount of EBA:

$$Y_{HEBA/EBA} = \frac{n_{HEBA,total,final}}{n_{EBA,available}} \tag{2.6}$$

For graphical representation of the molar balance, $n_{HEBA,total,k}$ and $n_{EBA,samples,k}$ were normalized by the reactor volume and plotted together with the in-reactor concentration $c_{EBA,k}$ in the result section.

3. Results and discussion

3.1. Preliminary investigation of electrochemical H_2O_2 generation

Prior to the electro-enzymatic batch process, co-substrate (H_2O_2) generation was quantified in enzyme-free, purely electrochemical experiments in the fluidized bed reactor. Building on our previous study [51], we now refine the potential window for efficient H_2O_2 formation relevant to the peroxygenase by evaluating applied potentials of −0.40, −0.47, −0.55 and −0.63 V vs. Ag/AgCl. Also, in this work, to intensify gas–liquid transfer and mixing for the electrochemical and the pursued combined electro-enzymatic process, air was now consistently supplied to the working electrode chamber at 73 mL/min ($k_La = 1.5$ 1/min). All experiments were performed under peroxygenase-compatible conditions (pH 6.1, 100 mM supporting electrolyte) in the working electrode chamber, under which the unspecific peroxygenase was confirmed to remain stable despite the applied aeration (see Fig. S5 in SI). The counter electrode chamber was maintained at acidic pH 3.1 with 250 mM supporting electrolyte. The resulting H_2O_2 generation rates and the current density over time are shown in Fig. 2A and B.

In the fluidized bed reactor H_2O_2 was successfully generated at the graphite electrode particles. Applying a more negative, cathodic potential (−0.40 to −0.63 V) increased the reduction of O_2 to hydrogen peroxide from 0.56 ± 0.04 to 1.87 ± 0.03 mM/h, enabling precise control of the H_2O_2 production rate via the applied potential. Consistent with the reduction potential, the average current density also became more negative, from −22 ± 5 to −70 ± 22 µA/cm^2 (compare Fig. 2B). Since current was normalized to the geometric electrode area, this increase in magnitude of the current density alongside the elevated H_2O_2 rate, indicates that a larger fraction of the fluidized electrode particles operated within a potential window favorable for electrochemical reduction of O_2 to H_2O_2. This current-potential relationship could be attributed to the inherent potential drop across the particle bed of the fluidized bed electrode due to particle-particle contact resistance [45,46,51]. As a consequence, particles located farther from the current feeder operated at more positive potentials than the applied potential at the current feeder. Thus, particularly at more positive potentials, a fraction of the particle bed did not reach the required overpotential for H_2O_2 formation and therefore did not contribute to O_2 reduction. At more negative applied reduction potentials, an increasing number of particles reached the required potential for oxygen reduction, thereby

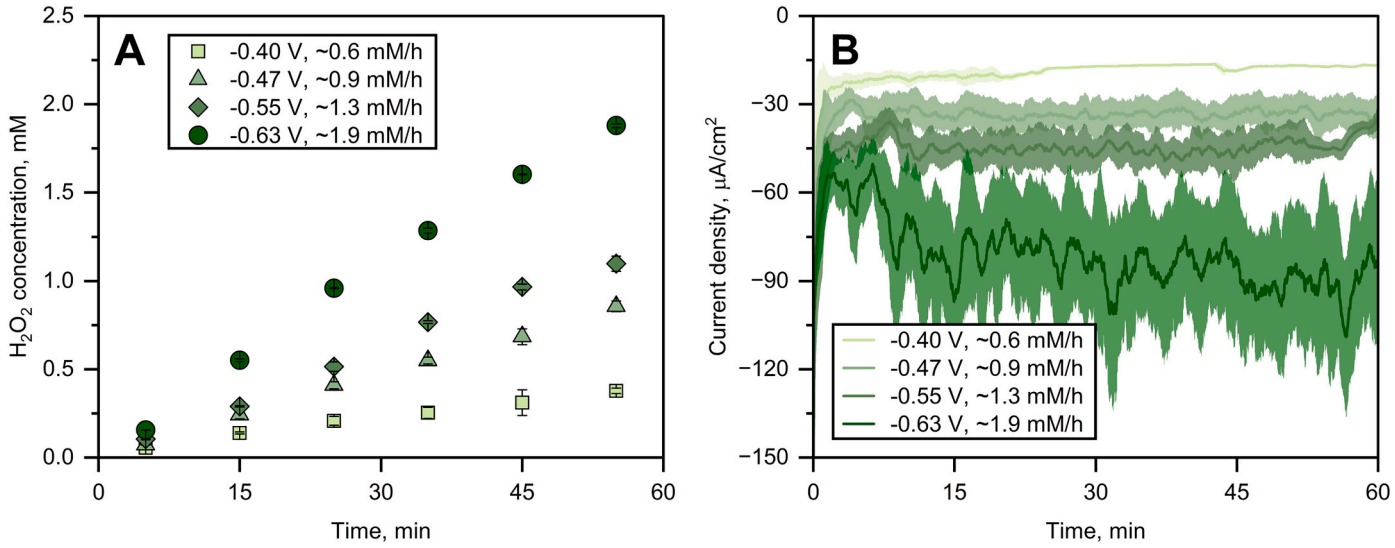

Fig. 2. Preceding electrochemical experiments to determine the in-situ generation of hydrogen peroxide for the electro-enzymatic process. In A the H_2O_2 concentration and in B the moving average of the current density are shown over time. The hydrogen peroxide generation was investigated at different applied potentials of −0.40, −0.47, −0.55 and −0.63 V vs. Ag/AgCl and H_2O_2 was measured in triplicates. Experiments were conducted, using 4.5 g of graphite particles (800–1200 µm), 100 mM potassium phosphate buffer at pH 6.1 and an air flow rate of 73 mL/min (k_La = 1.5 1/min) in the working electrode. A 250 mM potassium sulfate solution at pH 3.1 was utilized in the counter electrode chamber. The performance indicators of these preceding electrochemical H_2O_2 investigations are listed in Table S1 and Table S2 in SI.

leading to elevated H_2O_2 rates. In addition to this inherent resistance of the particle bed, intense air sparging, while beneficial for mixing and oxygen redelivery, caused rapid changes in the electrically connected fraction of the bed. This is reflected in the time-resolved current density, which exhibits superimposed oscillations. Two effects contribute to this behavior: (i) fluidized particles intermittently made or broke contact with one another or with the current feeder, (ii) gas bubbles temporarily attached to hydrophobic graphite surface, altering the available electroactive area in the reactor. Despite these current fluctuations, the H_2O_2 production rate remained stable over the investigated period, suggesting a dynamic steady state of the fluidized particle bed, and sufficient mixing by the aeration. Furthermore, we evaluated how efficient the current was converted into co-substrate. Under the enzyme friendly, near neutral pH of 6.1 and low salt concentration of 100 mM, competing side reactions, particularly further reduction of H_2O_2, were evident. The maximum current efficiency with 43.7 ± 11.9% was obtained at −0.47 V and a H_2O_2 production rate of 0.97 ± 0.09 mM/h, being slightly 4–5% higher than at −0.40 V and −0.55 V and within literature values reported for carbon materials at neutral pH (26.5–75.7%) [63]. At −0.63 V, the current efficiency dropped sharply to 16.4 ± 2.6% due to the onset of water electrolysis. These findings also align with our previous study [51], in which the platinized titanium current feeder itself (in the absence of graphite particles) exhibited only minor H_2O_2 formation (≤ 0.05 mM/h) and low current efficiencies (≤ 8.1%), while strongly promoting water splitting at potentials more negative than −0.55 V. Accordingly, although the cathodic window for oxygen reduction on the more selective graphite is not yet exhausted, the platinized current feeder limits overall system efficiency, particularly at more negative potentials due to enhanced water splitting. The operating potential therefore constitutes a trade-off between production rate and current efficiency. Even so, tuning the applied potential remains an effective means to precisely regulate co-substrate supply in the reactor. Overall, the fluidized bed reactor provides stable, well-mixed, co-substrate delivery at moderate current densities for the intended electro-enzymatic in-situ process. The full set of electrochemical performance indicators is provided in Table S1 in SI.

3.2. *Kinetic investigation of electro-enzymatic process conditions*

In addition to the electrochemical H_2O_2 generation, the kinetics of the EBA-to-HEBA conversion were characterized to identify the operating window of the combined electro-enzymatic process. Previous studies have shown that excessive hydrogen peroxide concentrations inhibit and deactivate unspecific peroxygenases [40,64–67]. Besides this widely investigated co-substrate inhibition, both insufficient or excessive educt concentrations may also slow reaction rates [39]. To balance these effects and maximize our production rates at practical EBA and H_2O_2 concentrations, we conducted a kinetic study to pinpoint feasible hydrogen peroxide concentrations and assess potential reactant inhibition effects. This study consisted of small-scale (1 mL) batch experiments, in which the reaction was halted within the initial linear period of enzymatic product generation using sodium azide. The results of these experiments are presented in Fig. 3A and B, showing the initial production rate of HEBA over the initial concentrations of EBA and H_2O_2 in the experiment. A maximum EBA concentration of 20 mM was used, as concentrations of 25 mM and higher proved to be incompletely soluble in the 100 mM potassium phosphate buffer of pH 6.1.

Fig. 3A shows that the unspecific peroxygenase exhibited substrate excess inhibition by both the co-substrate H_2O_2 and the educt EBA, as reflected by decreasing initial reaction rates at higher EBA and H_2O_2 concentrations, which deviates from classical Michaelis-Menten behavior. This is consistent with Bormann et al. [31], who likewise reported reduced initial reaction rates at elevated H_2O_2 or EBA concentrations, although in our case inhibition was more pronounced at pH 6.1 than reported in their study at pH 7. At EBA or H_2O_2 concentrations ≥ 15 mM, we observed initial rates remaining well below 50% of the maximum. The highest initial HEBA formation rates (≥ 7 mM/h) occurred for concentrations of 1–5 mM H_2O_2 and 1–5 mM EBA, with a maximum of 8.6 mM/h at 2.5 mM EBA and 2.5 mM H_2O_2. Although these H_2O_2 levels provided high initial reaction rates, they are rather unsuitable for sustained operation because they compromise enzyme stability and lead to accelerated deactivation of UPOs over time [39,67]. Consequently, unspecific peroxygenase-catalyzed systems typically employ in-situ H_2O_2 generation or controlled H_2O_2 delivery, in which the co-substrate is dosed just in the right amount, so that its bulk concentration remains close to zero (e.g. 0.06–0.28 mM [40] or 0.2–0.4 mM

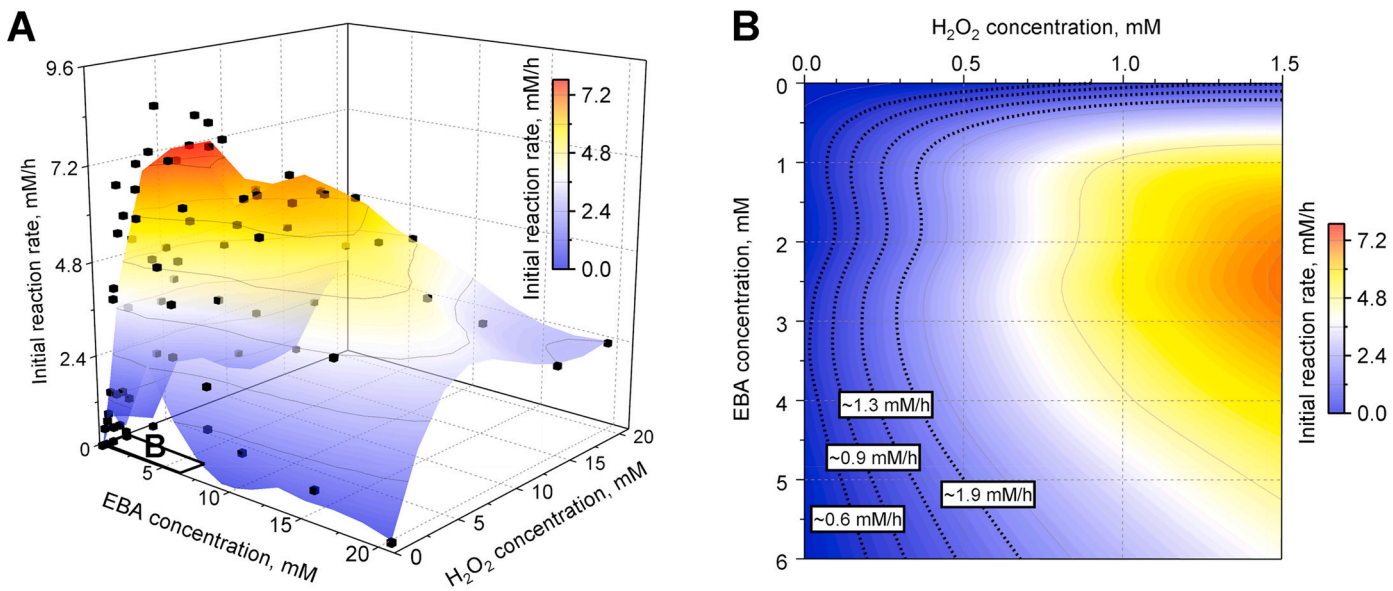

Fig. 3. Initial HEBA formation rates at varying initial EBA and H_2O_2 concentrations (0–20 mM) were determined in 1 mL batch experiments. Reactions were performed in 100 mM potassium phosphate buffer (pH 6.1) at room temperature, initiated by addition of 10.9 nM enzyme, and quenched after 60 s with 10 µL sodium azide. Each data point (filled black dot) represents an experimentally measured initial reaction rate in duplicates, and the color scale from blue to red indicates increasing initial HEBA reaction rates. A presents the entire investigated range as 3D plot, whereas B highlights a process-relevant section as 2D map. Dotted lines in B mark process windows where the theoretical achievable HEBA production rate matches or exceeds the determined potential-dependent H_2O_2 rate (~0.6–1.9 mM/h). Assuming no enzyme inactivation and constant H_2O_2 generation in an in-situ batch process, these intersections represent operating points at the respective EBA and H_2O_2 concentrations where H_2O_2 production and consumption to HEBA are balanced (stable operation).

[68]). In our kinetic investigation, initial reaction rates at low concentrations of either H_2O_2 or EBA also remained far below the maximum, and in addition, diminished with increasing imbalance of EBA:H_2O_2 ratio, e.g.: 1 mM EBA with 1 mM H_2O_2 yields ~64% of the maximum, 5/1 mM ~47%, 10/1 mM ~16% and 15/1 mM ~7%. Ergo, in-situ processes do not operate at the maximal achievable rates and depending on educt, substrate and enzyme concentration only certain rates are kinetically possible. Also, provided that no accelerated enzyme deactivation occurs, these trends indicate that maintaining a slight excess of H_2O_2 (e.g. up to 0.5 or 1 mM) can be beneficial for production rates, whereas strongly unbalanced conditions – with a large inhibitory excess of either reactant or with EBA driven toward near depletion – are unlikely to maximize catalytic turnover or volumetric productivity in the electro-enzymatic in-situ process. In principle, maintaining such a constant H_2O_2 excess under stable operation requires that the H_2O_2 production is not greater than the maximum achievable HEBA formation rate at the respective EBA, H_2O_2 and enzyme concentration [29].

For integration into the electro-enzymatic process, we selected 5 mM EBA as the starting concentration to remain within the kinetically favorable 1–5 mM range. Compared with EBA concentrations >5 mM at the same H_2O_2 concentration, this window yielded good initial HEBA rates already at low H_2O_2 concentrations (beneficial for enzyme stability). Fig. 3B isolates this process-relevant window from Fig. 3A and overlays for a stable process with constant production dotted lines onto the 2D HEBA rate field, indicating theoretical HEBA production rates that correspond to the previously determined potential-dependent H_2O_2 generation rates. At the investigated enzyme concentration, these lines map expected operating points of the in-situ process where enzymatic consumption matches or outperforms H_2O_2 production, indicating theoretical maximal HEBA rates at the respective EBA and H_2O_2 concentrations. In principle, assuming constant enzyme activity, a batch process would follow at a certain constant rate these dotted lines, spanning i.e. a theoretical process window. Under these ideal conditions with no enzyme inactivation, increasing the H_2O_2 supply shifts this production–consumption intersection in Fig. 3B (dotted lines) toward operating points with higher attainable HEBA rates, requiring also higher H_2O_2 levels at a given available EBA concentration. However, at the investigated enzyme concentration of 10.9 nM and the determined H_2O_2 generation rates (~0.6 mM/h to ~1.9 mM/h), these intersections lie near or above 0.2–0.3 mM H_2O_2, an upper threshold for enzyme stability, where deactivation has been reported to reduce TTNs for UPO-catalyzed systems [35,40]. Because Fig. 3 reports solely initial rates and UPO activity is known to inherently decay during catalysis [27,29,66], sustained operation in this regime is expected to necessitate a 2 to 3-fold higher enzyme concentration, assuming initial HEBA rates scale with enzyme concentration, which would move the process window (dotted lines) to lower H_2O_2 concentrations and provide an additional margin against deactivation over time. Nevertheless, initial rate kinetics alone cannot provide an assessment of enzyme stability or the enzyme concentration required for a respective conversion and instead both must be benchmarked at the experimentally determined H_2O_2 generation rates in the electrochemical fluidized bed reactor.

3.3. *Tuning H_2O_2 rates for the electro-enzymatic process: an enzyme-constrained approach*

To achieve high HEBA production rates and competitive total turnover numbers with the fluidized bed electrode, an optimal H_2O_2 generation rate is required. The rate must be high enough to sustain and maximize catalysis, while avoiding H_2O_2 excess accumulation that could destabilize the peroxygenase r*Aae*UPO. Guided by the preceding investigations in Sections 3.1 and 3.2, we benchmarked four different hydrogen peroxide generation rates (Fig. 4A: ~0.6 mM/h, B: ~1.0 mM/h, C: ~1.3 mM/h and D: ~1.9 mM/h) using comparable initial r*Aae*UPO concentrations of 20–24 ± 6 nM (~2× Fig. 3) at a pH value of 6.1 and an initial EBA concentration of ~5 mM EBA.

In Fig. 4A, a hydrogen peroxide generation rate of 0.56 ± 0.04 mM/h was applied at −0.40 V vs. Ag/AgCl, enabling steady hydroxylation of EBA to HEBA by the unspecific peroxygenase. By accounting for EBA and HEBA losses due to sampling, the mol balance was successfully closed. The HEBA production rate of 0.51 ± 0.01 mM/h aligned stoichiometrically with the consumption rates of EBA and H_2O_2 (~0.5–0.6

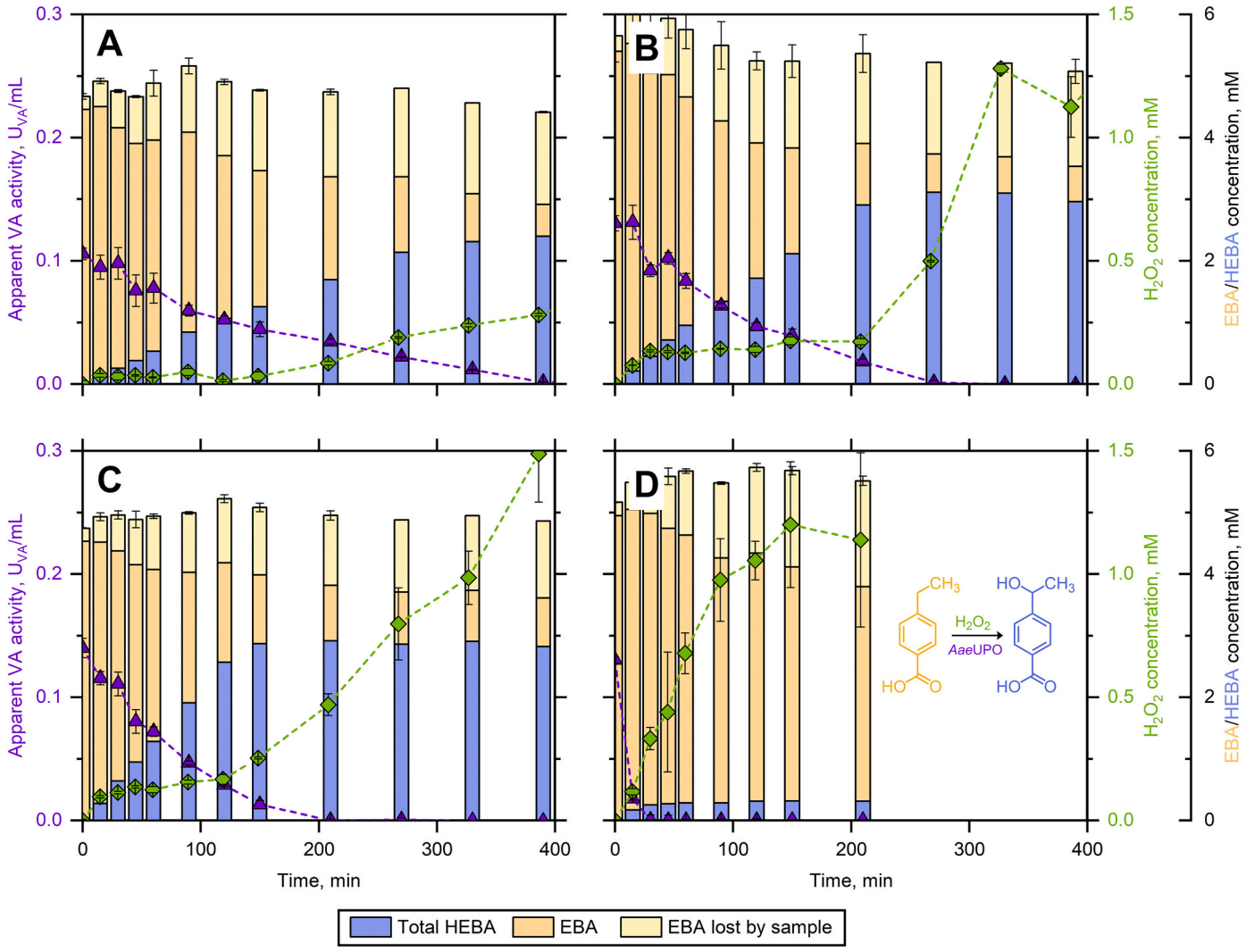

Fig. 4. Comparison of the electro-enzymatic catalysis of r*Aae*UPO (20–24 ± 6 nM) at different H_2O_2 generation rates (A: ~0.6 mM/h, B: ~1.0 mM/h, C: ~1.3 mM/h and D: ~1.9 mM/h), each with a similar initial apparent enzyme activity of approximately 0.11–0.13 U_{VA}/mL. Experiments were conducted, using 4.5 g of graphite particles (800–1200 µm), 100 mM potassium phosphate buffer at pH 6.1 and an air flow rate of 73 mL/min (k_La = 1.5 1/min) in the working electrode chamber. A 250 mM potassium sulfate solution at pH 3.1 was utilized in the counter electrode chamber. For representation, the mol balance for EBA and HEBA was closed. The cumulative loss due to sampling was separately highlighted for EBA as a loss (yellow), accounted for within the total concentration for HEBA (blue) and displayed together with the concentration of EBA in the reactor (orange). Additionally, the H_2O_2 concentration (green) and the apparent residual activity toward the model substrate VA (purple) are shown. During batch operation, samples were directly taken from the reactor, and the sampled volume refilled with buffer without EBA and without enzyme. Samples for EBA/HEBA and H_2O_2 analysis were deactivated by sodium azide.

mM/h), confirming that the co-substrate was exclusively used for the hydroxylation of EBA to HEBA. At this production rate, the hydrogen peroxide concentration in the reactor volume remained close to 0 mM until approximately 150 min. A small excess of H_2O_2 became detectable at 210 min, with one-third of the initial apparent enzyme activity still active. Complete enzyme inactivation occurred at 400 min, yielding a total HEBA concentration of 2.54 mM, including losses due to sampling. Nevertheless, throughout the process, H_2O_2 concentrations stayed below 0.3 mM, indicating an in-situ production, where co-substrate generation matched enzymatic consumption for the EBA to HEBA conversion. Despite this, a steady decrease in apparent veratryl alcohol activity was observed. This decline can be attributed to a combination of enzyme dilution due to sampling and turnover-dependent enzyme inactivation. The latter is consistent with the known behavior of unspecific peroxygenases, which, in addition to productive catalysis, can undergo H_2O_2-driven side reactions (e.g., catalase-like dismutation to water and oxygen) leading to oxidative heme damage and loss of activity [66]. Although limited at low bulk H_2O_2 levels, such pathways still occur at a slow rate and are expected to accelerate with excess H_2O_2 accumulation [66]; however, no such acceleration was observed in Fig. 4A. Control experiments exhibited no significant loss of activity over 240 min under air sparging conditions (73 mL/min, k_La = 1.5 1/min) and potential shear stress from electrode particles, compared to a reference without air sparging (see Fig. S5 in SI), indicating that the observed activity decrease is not caused by external process effects. At the end of the process in Fig. 4A, 0.52 mM of EBA remained in the reactor resulting in a yield of 82%, indicating the applied enzyme amount may be the limiting factor for achieving complete conversion of the available EBA to HEBA. The extended process time of 400 min, coupled with the low reaction rate, resulted in also considerable enzyme and EBA losses and dilution due to sampling (1.7 mL per sample compared to 35 mL reactor volume), reducing enzyme activity and EBA concentration in the reactor. This depletion likely affected the kinetics of HEBA generation toward the later stages of the process, yielding 2.54 mM HEBA compared to the ~3.1 mM EBA available in total for conversion. At a nearly constant H_2O_2 generation rate, both the enzyme activity depletion and the

following lower achievable HEBA rate, lead to a necessary small excess of H_2O_2 toward the end of the process, as depicted in the time resolved process kinetics in Fig. S1 (based on Fig. 3). While these factors contribute to the observed limitations, the primary constraint on entire HEBA production is the insufficient H_2O_2 generation rate, which failed to support higher production rates.

When the hydrogen peroxide rate was increased to 0.97 ± 0.09 mM/h at −0.47 V vs. Ag/AgCl in Fig. 4B, the HEBA generation rate rose correspondingly to 0.84 ± 0.08 mM/h. During the first 30 min an excess of ~0.15 mM hydrogen peroxide formed, which remained around this level until 200 min in the process, suggesting a stationary state resulting from H_2O_2 generation and its consumption via EBA hydroxylation to HEBA. This can be seen even better in the time-resolved analysis of the process kinetics, showing a production–consumption balance near ~0.15 mM H_2O_2 during this time (Fig. S2, based on Fig. 3). Due to the increased H_2O_2 rate, the matching HEBA rate required in the stationary state a slightly elevated H_2O_2 concentration, making this a kinetic bulk effect and not an effect arising from insufficient mixing, as most of the H_2O_2 generation happens at the lower reactor section, where the majority of the particle electrode is located. Between 210 and 270 min, once EBA decreased to ≤1 mM and the apparent enzyme activity dropped below 0.02 U_{VA}/mL, the operation point in the reactor shifted to higher H_2O_2 concentrations. This resulted in a sharp hydrogen peroxide accumulation of 0.50 mM, which was not beneficial for enzyme stability and potentially deactivated the enzyme during the final phase of the process. In this regime with low remaining active enzyme and reduced EBA concentrations, the enzyme was falling short kinetically as even increasing H_2O_2 concentrations did not help to maintain the HEBA formation rate, causing the HEBA rate to drop from ~0.9 mM/h to ~0.5 mM/h (i.e. tipping point), and consequently H_2O_2 to rise due the lowered H_2O_2 consumption (Fig. S2). This sharp rise in H_2O_2 concentration in turn further promoted deactivation of the enzyme until no enzyme activity was left. Despite the late-stage H_2O_2 excess, the enzyme effectively handled the elevated H_2O_2 generation rate and performance improved overall relative to Fig. 4A (H_2O_2 rate 0.56 ± 0.04 mM/h). HEBA reached a total concentration of 3.15 mM, higher than in Fig. 4A, owing to the combination of slightly higher initial apparent enzyme activity (0.13 vs. 0.11 U_{VA}/mL) and the higher H_2O_2 supply rate, which accelerated conversion and shortened the process time from 390 to 270 min. The process achieved a yield of 80%, allowing the assumption that the initial enzyme amount may have been globally sufficient, but due the described effects e.g. negative influence of dilution on the kinetics, full conversion was not achievable at this applied enzyme concentration.

In Fig. 4C, a hydrogen peroxide rate of 1.27 ± 0.02 mM/h (−0.55 V vs. Ag/AgCl) was applied, resulting in an initial HEBA production rate of 1.10 ± 0.02 mM/h. Although this HEBA production rate was significantly lower than the electrochemical H_2O_2 generation rate, hydrogen peroxide concentration remained slightly below 0.2 mM during the first 120 min, indicating near on-demand utilization at the start of the process. The increased H_2O_2 delivery improved the HEBA production rate, allowing the process to conclude in less time at 210 min with no remaining enzyme activity. Owing to the higher reaction rates compared to Fig. 4A and B, less EBA was lost through sampling. Additionally, this reduced sampling loss helped to maintain an EBA surplus of more than ~0.9 mM over the entire process, which together with the small excess of H_2O_2 likely further benefited the reaction rate kinetically (see Fig. S3). However, as the apparent enzyme activity dropped to 0.03 U_{VA}/mL at 120 min, the hydrogen peroxide concentration started to further increase. Due to a presumably lower H_2O_2 consumption, a higher difference between H_2O_2 rate and HEBA production than initially reported was apparent. Between 150 and 210 min at elevated hydrogen peroxide concentrations exceeding 0.2–0.3 mM, no further hydroxylation to HEBA was observed, despite seemingly sufficient apparent enzyme activity and available EBA. Based on the time-resolved kinetic analysis in Fig. S3, at this stage close to 1 mM EBA and low remaining enzyme activity, substantially higher H_2O_2 concentrations than observed would have been necessary to uphold a HEBA production or H_2O_2 consumption rate identical to the start (~1.1–1.3 mM/h), making a stable process point kinetically unattainable (achievable ~0.5 mM/h) and resulting in further H_2O_2 accumulation. Presumably, at this point (~150 min), the imbalance between H_2O_2 supply and productive turnover likely shifted the enzyme response toward non-productive pathways, e.g. catalase malfunction, which is the enzyme's inherent mechanism to cope with the rising H_2O_2 amounts [29,66], leading to progressive inactivation and resulting in negligible HEBA formation. In addition, local H_2O_2 concentrations at the electrode surface were likely higher than the bulk values reflected by the measurement from the top of the reactor. This localized increase, along with possible pH shifts directly at the particle surface caused by proton consumption during oxygen reduction, could have also contributed to reduced enzyme stability, despite the bulk electrolyte being buffered. By 210 min, the HEBA concentration reached a final value of 2.96 mM, corresponding to a yield of 77%. Here, the HEBA amount was slightly lower than in Fig. 4B (H_2O_2 generation rate of 0.97 ± 0.09 mM/h), consistent with the reduced ability of the enzyme to tolerate and productively utilize the elevated H_2O_2 concentrations in Fig. 4C.

In Fig. 4D, a hydrogen peroxide generation rate of 1.87 ± 0.03 mM/h was applied, which resulted in a HEBA production rate of only 0.68 ± 0.02 mM/h. As these initial production rates are determined during the first 15 min, this immediate mismatch indicated evidently that the enzyme could not handle the elevated H_2O_2 supply from the beginning. Rapid enzyme inactivation occurred within the first 30 min, yielding a HEBA concentration of just 0.32 mM HEBA. Consequently, no on-demand balance was established between H_2O_2 consumption and production, as the excess H_2O_2 accumulated throughout the process. Notably, the initial rise in excess H_2O_2 of ~0.60 mM/h did not correspond with the applied generation rate determined in prior pure electrochemical experiments minus the HEBA production rate, i.e., the combined mass balance of HEBA and H_2O_2 formation could not be closed. This deviation suggests that the enzyme consumed H_2O_2 in non-productive reactions during inactivation. Interestingly, Karich et al. reported a TTN of 12,500 mol/mol for the "pure" catalase activity of *Aae*UPO (i.e. with H_2O_2 as sole substrate) [66]. Given that the initially applied enzyme was inactivated within 30 min (Fig. 4D), a comparable catalase-type response under excessive H_2O_2 would correspond to a H_2O_2 consumption rate of ~0.5–0.6 mM/h. Together with irreversible loss of peroxygenase activity via heme-bleaching and/or protein oxidation, such non-productive consumption could explain the observed mass balance gap and initially suppress the measured bulk H_2O_2 concentration. Moreover, enzymes near the electrode surface may have encountered even higher H_2O_2 levels. Close to the H_2O_2 origin, this could create a self-accelerating effect as the inactivation near the electrode surface would lower the amount of active enzyme locally, which in turn would further exacerbate the kinetically unfavorable mismatch between local co-substrate supply and enzymatic capacity, accelerating inactivation faster than active enzyme could be replenished by mixing due to aeration, ultimately inactivating all remaining active enzyme. These interpretations are generally supported by the time-resolved kinetic analysis in Fig. S4 in SI, which suggests that at the applied H_2O_2 rate, the EBA hydroxylation rates required for an on-demand regime should have been kinetically achievable given the amount of enzyme, EBA and H_2O_2 concentrations (Fig. S4B). However, as H_2O_2 accumulated (Fig. S4C), enzyme activity declined faster than the rising H_2O_2 levels could kinetically compensate for (i.e., by increasing the maximal achievable HEBA rates), preventing the establishment of a production-consumption balance as observed in Fig. 4A-C and instead leading to complete peroxygenase inactivation and rapid H_2O_2 accumulation. Furthermore, this rapid inactivation effect may have been intensified by reactive oxygen species formation at the potential of −0.63 V, as superoxide, hydroxyl and hydroperoxyl radicals have been proposed during oxygen reduction under certain conditions [41,69,70]. At a higher current density and given the lower reported current efficiency

for H_2O_2 generation (see Section 3.1), additional electrochemical side reactions could also have induced pH-shifts at the electrode particle surface, inhibiting the enzyme locally and further accelerating inactivation.

To get a better overview of the key performance indicators of the batch processes, parameters such as the STY_{HEBA}, current density, current efficiency, TTN and the production rates were calculated and summarized in Table 1. STY_{HEBA} was calculated based on the volume occupied by the electrode particles, whereas the production rates were referenced to the electrolyte volume. For direct comparability, current density, current efficiency, production rate, and STY_{HEBA} were evaluated at 15 min into the experiments. Additional performance data for both the electro-enzymatic system and the electrochemical H_2O_2 generation control are provided in Tables S1, S3, and S5 in the SI.

Consistent with the observed HEBA production rates, the STY_{HEBA} increased with the applied H_2O_2 generation rate up to the highest level that the enzyme could still tolerate without immediate inactivation. This maximum STY_{HEBA} of 21.96 ± 0.01 g/(L·d) was obtained in Fig. 4C. At lower H_2O_2 rates, the STY_{HEBA} decreased to 16.76 ± 1.69 g/(L·d) in Fig. 4B and 10.20 ± 0.15 g/(L·d) in Fig. 4A, as less hydrogen peroxide was available for the hydroxylation of EBA to HEBA. Where the H_2O_2 generation rate exceeded the enzyme's consumption capacity (Fig. 4D), rapid enzyme inactivation curtailed overall product formation, although an initial STY_{HEBA} of 13.47 ± 0.30 g/(L·d) was still observed.

To evaluate charge utilization, current efficiencies determined for H_2O_2 generation in the electrochemical controls (Section 3.1, Table S1 in SI) were compared with HEBA-based current efficiencies of the coupled electro-enzymatic system, in which in-situ generated H_2O_2 was consumed by the peroxygenase. Notably, across Fig. 4A-C, HEBA current efficiencies were slightly higher (3–11%) than H_2O_2 efficiencies in purely electrochemical controls, indicating that coupling H_2O_2 generation to an enzyme sink may improve charge utilization. In the electro-enzymatic process, the highest HEBA current efficiency of 54.5 ± 12.5% was observed in Fig. 4B (−0.47 V vs. Ag/AgCl), exceeding the corresponding electrochemical H_2O_2 control of 43.7 ± 11.9% at −0.47 V vs. Ag/AgCl. This suggests that enzymatic consumption may benefit the electrochemical reaction, likely by suppressing electrochemical side reactions to some extent, e.g. four-electron oxygen reduction and further reduction of H_2O_2 to water, that lower H_2O_2 efficiency and become more prominent at higher peroxide levels. Accordingly, the lower H_2O_2 concentrations in the in-situ electro-enzymatic process likely reduced these losses and increased the current efficiency for H_2O_2 and thus HEBA formation. Overall, HEBA current efficiencies followed the potential-dependent trends of electrochemical H_2O_2 generation (see Section 3.1, Table S1 in SI), indicating that efficiency was mainly dictated by the electrochemical step. At the more positive potential of −0.40 V in Fig. 4A, the HEBA current efficiency of 41.2 ± 5.0% was lower compared to Fig. 4B despite near-complete enzymatic consumption of the produced hydrogen peroxide. This is consistent as due to the inherent potential-drop within the fluidized bed, comparably less graphite particles operated at ORR potential and the less-suited platinized current feeder contributed more strongly, lowering selectivity toward H_2O_2 and consequently reducing HEBA current efficiency in the combined system. In Fig. 4C, at the more negative potential of −0.55 V vs. Ag/AgCl, additional electrochemical side reactions could have become relevant, e.g. hydrogen evolution at the platinized current feeder, reducing the H_2O_2 and thus HEBA current efficiency to 43.0 ± 8.3%. Moreover, the slight mismatch between H_2O_2 production and enzymatic consumption, as indicated in the slowly gradual rise in H_2O_2 concentration over time in Fig. 4C, still left room for a theoretical higher achievable HEBA current efficiency, as that fraction of charge contributed from the process start to H_2O_2 accumulation rather than productive conversion to HEBA.

The TTN_{HEBA}, showing overall catalytic productivity per enzyme, exhibited the expected trade-off between enzyme stability and H_2O_2 exposure. TTN_{HEBA} was highest in Fig. 4A with 188,900 ± 50,000 mol/mol, where the lowest hydrogen peroxide production rate at −0.40 V vs. Ag/AgCl minimized local H_2O_2 concentrations and the H_2O_2-limited environment ensured the most stable enzyme performance. TTN_{HEBA} decreased marginally to 178,800 ± 48,000 mol/mol in Fig. 4B and to 170,800 ± 44,300 mol/mol in Fig. 4C, consistent with increased peroxide stress, particularly toward the end of the process when H_2O_2 accumulated at low EBA concentrations. A controlled but drastic reduction of the H_2O_2 generation rate toward the end of the batch process could, in principle, mitigate late-stage inactivation and increase conversion and TTN_{HEBA} at the investigated enzyme concentration [39,40]. However, such a strategy would prolong the overall process time [39,40]. Indeed, complete hydroxylation of the remaining EBA would correspond to a theoretical maximum TTN of up to ~230,000 mol/mol (see Table S5 in SI). In Fig. 4D, the highest H_2O_2 rate at −0.63 V vs. Ag/AgCl resulted in rapid enzyme inactivation, yielding negligible product formation and consequently, the lowest TTN_{HEBA} of 15,000 ± 4300 mol/mol.

3.4. Pushing electro-enzymatic production: an enzyme-surplus approach

So far, the H_2O_2 generation rate and its influence on enzyme performance was investigated at a single enzyme concentration (~2× Fig. 3). By pushing the H_2O_2 generation rate beyond the enzyme's on-demand capacity, we identified performance limitations imposed by the available enzyme amount. To address these constraints, the enzyme concentration in the batch process was increased to 30–34 ± 9 nM (~3× Fig. 3), raising apparent enzyme activity from 0.11–0.13 U_{VA}/mL to 0.19–0.20 U_{VA}/mL, while keeping all other conditions constant. In Fig. 5A, a hydrogen peroxide generation rate of 0.9 mM/h was applied, comparable to Fig. 4B, to aim for an enhanced conversion. In Fig. 5B, a higher hydrogen peroxide generation rate of 1.9 mM/h was selected, a rate that previously caused enzyme inactivation (as indicated in Fig. 4D) to benchmark and evaluate the possibility to further intensify the production rate in the process.

The increased enzyme concentration (see Fig. 5A) enabled complete conversion of the available EBA ($Y_{HEBA/EBA}$ ~100%) by 270 min, yielding 3.97 mM HEBA. During the experiment, 1.29 mM EBA was removed by sampling. Throughout the productive phase, H_2O_2 accumulation remained low (0.05 to 0.10 mM), reaffirming on-demand production in which electrochemical H_2O_2 generation was in balance

Table 1
Summary of the performance indicators determined for the electro-enzymatic process with an apparent enzyme activity of 0.11–0.13 U_{VA}/mL. The current, the current efficiency, the production rate, and the space time yield are shown at 15 min of the experiments. The space time yield is based on the occupied particle electrode volume, whereas the production rate considers the complete working electrode chamber volume. The TTN was calculated for the entire process with sampling based on eqs. (S2.5-S2.7). Additional performance data for both the electro-enzymatic process and the electrochemical hydrogen peroxide control are provided in Tables S1, S3 and S5 in SI. All parameters for the calculations were measured in triplicates.

Figure	Potential vs. Ag/AgCl, V	H_2O_2 rate, mM/h	HEBA rate, mM/h	Φ^e_{HEBA}, %	Current density, μA/cm²	TTN_{HEBA}, mol/mol	STY_{HEBA}, g/(L•d)
4A	−0.40	0.56 ± 0.04	0.51 ± 0.01	41.2 ± 5.0	−19 ± 2	188,900 ± 50,000	10.20 ± 0.15
4B	−0.47	0.97 ± 0.09	0.84 ± 0.08	54.5 ± 12.5	−24 ± 5	178,800 ± 48,000	16.76 ± 1.69
4C	−0.55	1.27 ± 0.02	1.10 ± 0.02	43.0 ± 8.3	−40 ± 8	170,800 ± 44,300	21.96 ± 0.01
4D	−0.63	1.87 ± 0.03	0.68 ± 0.02	16.3 ± 3.3	−64 ± 13	15,000 ± 4300	13.47 ± 0.30

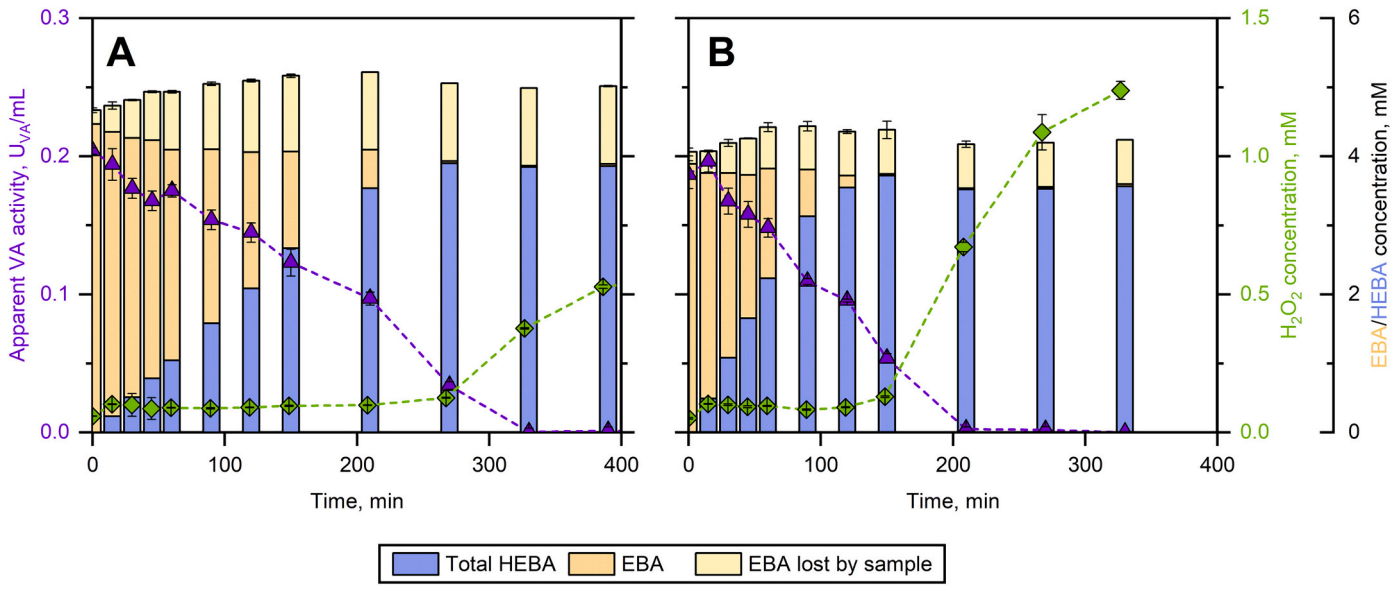

Fig. 5. Comparison of the electro-enzymatic catalysis of r*Aae*UPO (30–34 ± 9 nM) at different H_2O_2 generation rates (A: ~0.9 mM/h and B: ~1.9 mM/h), each with a similar initial apparent enzyme activity of approximately 0.19–0.20 U_{VA}/mL. Experiments were conducted, using 4.5 g of graphite particles (800–1200 µm), 100 mM potassium phosphate buffer at pH 6.1 and an air flow rate of 73 mL/min (k_La = 1.5 1/min) in the working electrode. A 250 mM potassium sulfate buffer at pH 3.1 was utilized in the counter electrode chamber. For representation, the mol balance for EBA and HEBA was closed. The cumulative loss due to sampling was separately highlighted for EBA as a loss (yellow), accounted for within the total concentration for HEBA (blue) and displayed together with the concentration of EBA in the reactor (orange). Additionally, the H_2O_2 concentration (green) and the apparent residual activity toward the model substrate VA (purple) are shown. In batch operation, samples were directly taken from the reactor, and the sampled volume refilled with buffer without EBA and without enzyme. Samples for EBA/HEBA and H_2O_2 analysis were deactivated using sodium azide.

with its consumption via enzymatic hydroxylation. Consistently, the applied H_2O_2 generation rate closely matched the HEBA formation rate of 0.94 ± 0.01 mM/h. The slightly lower hydrogen peroxide levels compared with Fig. 4B were consistent with the higher enzyme concentration, as lower H_2O_2 levels were kinetically sufficient to sustain similar formation rates. After 210 min, the HEBA production rate started to decrease due to diminishing EBA concentrations, accompanied by rapid loss of apparent enzyme activity. This likely reflects local EBA limitation within the reactor, exposing the enzyme predominantly to H_2O_2 and promoting inactivation. By 330 min, enzyme activity was no longer detectable, and H_2O_2 began to accumulate. The resulting STY_{HEBA} of 18.62 ± 0.16 g/(L•d) (Fig. 5A) was comparable to Fig. 4B with a STY_{HEBA} of 16.76 ± 1.69 g/(L•d), consistent with identical H_2O_2 generation rates. Overall, despite producing similar amounts of HEBA per applied enzyme compared to Fig. 4B, ~0.05 U_{VA}/mL of apparent enzyme activity remained after full available EBA conversion ($Y_{HEBA/EBA}$ ~100%). In addition, enzyme performance appeared improved relative to Fig. 4B, as the non-sampling-related activity loss was lower during productive catalysis. Given identical sampling volumes, sampling accounted for a larger fraction of total activity loss (~0.07 U_{VA}/mL in Fig. 5B vs. ~0.03 U_{VA}/mL in Fig. 4B, with a similar total decrease of ~0.10–0.11 U_{VA}/mL during first 210 min), implying proportionally reduced inactivation alongside increased product formation. These findings demonstrate that adding more enzyme supported higher robustness and enabled complete conversion of the available EBA under otherwise identical reaction conditions. Moreover, the residual apparent enzyme activity after full EBA consumption suggests that additional EBA supplementation could further increase the final product titer. Especially, since the achieved TTN_{HEBA} of 188,200 ± 48,800 mol/mol reached the theoretical maximum under these batch conditions, which means that TTN_{HEBA} was capped by the amount of EBA available in the process (see Table S6 in SI).

In Fig. 5B, we investigated whether the additional enzyme concentration could not only ensure a $Y_{HEBA/EBA}$ of 100% but also enable enhanced production rates (i.e., the STY) at a H_2O_2 generation rate that previously caused rapid enzyme inactivation (as shown in Fig. 4D). A H_2O_2 generation rate of 1.91 ± 0.05 mM/h was applied, and complete conversion of the available EBA was reached after 150 min, i.e., in approximately half the time required in Fig. 5A. The final HEBA concentration was 3.79 mM, with 0.73 mM EBA lost by sampling. Here, a lower initial EBA concentration (~4.50 mM) was applied and ~0.08 U_{VA}/mL of apparent enzyme activity remained at the time of complete EBA consumption. After 120 min, approximately half of the apparent enzyme activity (~0.10 U_{VA}/mL) had been lost. Sampling alone accounted for ~0.05 U_{VA}/mL of this decrease, indicating that a substantial fraction of the measured activity loss was experimental rather than inactivation related. The process in Fig. 5B achieved the highest HEBA production rate of 1.95 ± 0.02 mM/h. Between 90 and 150 min, the HEBA formation rate decreased, which was consistent with the decline to kinetically unfavorable EBA concentrations below 1.0 mM. As in Fig. 5A, the H_2O_2 concentrations remained at a low concentration (<0.1 mM) throughout the productive phase and increased sharply only after enzyme activity loss, reaching concentrations higher than 1.2 mM. Overall, Fig. 5B demonstrated efficient in-situ co-substrate generation with on demand H_2O_2 generation for the enzyme. Adding more enzyme significantly improved yield and production rate, resulting in the highest STY_{HEBA} for HEBA of 38.83 ± 0.32 g/(L·d). In contrast, TTN_{HEBA} remained limited by the amount of available EBA, maxing out at 143500 ± 37,600 mol/mol (compare theoretical maximal TTN in Table S6 in SI). At the elevated potential of −0.63 V vs Ag/AgCl, the current efficiency dropped to 18.9 ± 3.2%, consistent with increased electrochemical side reactions, i.e., hydrogen evolution at the platinized current feeder.

Key performance indicators for Fig. 5A and B are listed in Table 2 (see also Tables S2, S4 and S6 in the SI for additional performance data). As before, the STY_{HEBA} was calculated based on the volume occupied by the electrode particles, whereas the production rate was referenced to the electrolyte volume. For direct comparability, current density, current efficiency, production rate and STY_{HEBA} were evaluated at 15 min. In both our processes, measurable apparent enzyme activity remained of around ~0.05 and ~0.08 U_{VA}/mL at the time of complete EBA

Table 2
Summary of the performance indicators determined for the electro-enzymatic process with an apparent enzyme activity of 0.19–0.20 U_{VA}/mL. The current density, the current efficiency, the production rate, and the space time yield are shown at 15 min of the experiments. The space time yield is based on the occupied particle electrode volume, whereas the production rate considers the volume of the working electrode chamber. The TTN was calculated for the entire process with sampling based on eqs. (S2.5-S2.7). Additional performance data for both the electro-enzymatic process and the electrochemical hydrogen peroxide control are provided in Tables S2, S4 and S6 in SI. All parameters for the calculations were measured in triplicates.

Figure	Potential vs. Ag/AgCl, V	H_2O_2 rate, mM/h	HEBA rate, mM/h	Φ^e_{HEBA}, %	Current density, μA/cm^2	TTN_{HEBA}, mol/mol	STY_{HEBA}, g/(L•d)
A	−0.47	0.86 ± 0.01	0.94 ± 0.01	38.2 ± 4.9	−38 ± 5	188,200 ± 48,800	18.62 ± 0.16
B	−0.63	1.91 ± 0.05	1.95 ± 0.02	18.9 ± 3.2	−159 ± 27	143,500 ± 37,600	38.83 ± 0.32

consumption. If this residual apparent activity had performed similarly and at rates comparable to the initial ~0.10 U_{VA}/mL under non-limiting substrate (EBA and H_2O_2) availability, the TTN_{HEBA} could have theoretically increased to approximately ~340,000 mol/mol for both Fig. 5A and Fig. 5B, approaching values reported in literature for similar electro-enzymatic processes. For example, using the same EBA-HEBA reaction system and unspecific peroxygenase (12.5 nM r*Aae*UPO), Bormann et al. showcased and modeled a gas diffusion electrode (GDE) system for in-situ H_2O_2 generation reaching a maximal TTN of up to ~400,000 mol/mol at ~1.3 mM/h [39]. Sayoga et al. reported TTNs of ~220,000 mol/mol (30 nM r*Aae*UPO) and ~450,000 mol/mol (10 nM r*Aae*UPO) at a formation rate of ~0.24 mM/h using an all-in-one electrode [30]. However, the highest TTN of 710,000 mol/mol (10 nM r*Aae*UPO) at efficiencies of up to 55% has been reported in a H_2O_2 sensor-controlled GDE-setup for this electro-enzymatic reaction system [40]. Overall, in our fluidized bed reactor, the formation rates and current efficiencies were comparable to these processes in the literature, while the achieved STY_{HEBA} was among the highest, only approached by Bormann et al. (estimated ~28 g/(L•d)) [39], highlighting the key advantage of the fluidized bed reactor configuration for electro-enzymatic synthesis.

To translate these higher TTNs into practice in our reactor, two limitations must be addressed: the late-stage enzyme inactivation caused by a high H_2O_2–rate to enzyme capacity mismatch (Fig. 4), and EBA substrate depletion and local limitation toward the end of the process (Fig. 5), which kinetically reduced the formation rate and promoted inactivation. From a process standpoint, these challenges could be overcome by dynamically controlling the H_2O_2 generation rate and supplying EBA continuously (or in a semi-batch mode). Such strategies are also electrochemically advantageous, as continuous operation in the fluidized bed reactor has been shown to improve current efficiency and to prevent pronounced pH shifts caused by electrochemical oxygen reduction [51], thereby helping to maintain conditions favorable for enzyme stability and productivity.

4. Conclusion and outlook

Electro-enzymatic syntheses require scalable electrode designs that can seamlessly integrate electrochemical and biological processes. In this work, we demonstrate, for the first time, the successful application of an electrochemical fluidized bed reactor to an electro-enzymatic synthesis. By combining the favorable mixing properties of a fluidized bed with the high volume-specific electrode surface of particle electrodes, high space-time yields and robust total turnover numbers were achieved in batch operation.

A key factor in realizing this performance in the fluidized bed reactor was the ability to maintain the in-situ hydrogen peroxide concentration below inhibitory levels. At a fixed enzyme concentration, this was done by optimizing the H_2O_2 generation rate via the applied potential based on preceding electrochemical investigations of the H_2O_2 production and based on studies on the reaction kinetics of the enzymatic hydroxylation of EBA to HEBA, both at a pH value of 6.1. When increasing the enzyme concentration, the electro-enzymatic system could be pushed to even higher space-time yields at $Y_{HEBA/EBA}$ ~100%. In the fluidized bed reactor space-time yields of up to 38.83 ± 0.32 g/(L•d) and current efficiencies reaching up to 54.5 ± 12.5% were attained. While demonstrated at laboratory scale, consistent scale-up will require careful control of fluidization behavior, current and potential distribution, and in-situ H_2O_2 generation to minimize gradients and sustain reactor performance. Extension of this concept to other peroxygenases or co-substrate-dependent enzymes will require adapting reaction conditions to ensure enzyme and co-substrate stability, particularly for halide-dependent systems where hypohalite intermediates may be sensitive to gas–liquid mass transfer.

Future improvements could focus on enhancing current efficiency through more efficient electrochemical catalysts and boosting enzyme performance by further optimizing reaction conditions, mainly salt concentration and pH, as well as by immobilizing the enzymes for enhanced stability. Alongside these measures, STYs could be further increased by raising in-situ H_2O_2 generation rates, for example via improved oxygen transport to the electrode surface. However, the primary kinetic limitations persist in substrate inhibition at high EBA concentrations and EBA's limited solubility, challenges that could be addressed by continuous or semi-batch reactor configurations that enable effective EBA resupply.

CRediT authorship contribution statement

Michael Abt: Writing – review & editing, Writing – original draft, Visualization, Project administration, Methodology, Data curation, Conceptualization. **Carolin Kienzle:** Visualization, Methodology, Data curation. **Melissa Ditzel:** Visualization, Methodology, Data curation. **Mirco Jestädt:** Methodology, Data curation. **Katharina Bleher:** Writing – review & editing, Methodology. **Matthias Franzreb:** Writing – review & editing, Supervision, Project administration, Funding acquisition. **André Tschöpe:** Writing – review & editing, Writing – original draft, Project administration, Funding acquisition, Conceptualization.

Declaration of generative AI and AI-assisted technologies in the writing process

During the preparation of this work the authors used ChatGPT in order to improve the readability and language of the manuscript. After using this tool, the authors reviewed and edited the content as needed and take full responsibility for the content of the published article.

Declaration of competing interest

The authors declare that they have no known competing financial interests or personal relationships that could have appeared to influence the work reported in this paper.

Acknowledgements

This work was performed within the project “Bioelectrochemical and engineering fundamentals to establish electro-biotechnology for biosynthesis - Power to value-added products (eBiotech)” funded by the Deutsche Forschungsgemeinschaft (DFG) - project number 445807856. We thank Frank Hollmann and Dirk Holtmann for providing the enzyme

used in this work. Furthermore, we acknowledge Miquel Alcalde and his research group for developing the PaDa-I variant of *Aae*UPO.

Appendix A. Supplementary data

Supplementary data to this article can be found online at https://doi.org/10.1016/j.cej.2026.177731.

Data availability

Data will be made available on request.

References

[1] A. Schmid, J.S. Dordick, B. Hauer, A. Kiener, M. Wubbolts, B. Witholt, Industrial biocatalysis today and tomorrow, Nature 409 (2001) 258–268, https://doi.org/10.1038/35051736.

[2] E.L. Bell, W. Finnigan, S.P. France, A.P. Green, M.A. Hayes, L.J. Hepworth, S. L. Lovelock, H. Niikura, S. Osuna, E. Romero, K.S. Ryan, N.J. Turner, S.L. Flitsch, Biocatalysis, Nat. Rev. Methods Primers 1 (2021) 46, https://doi.org/10.1038/s43586-021-00044-z.

[3] M.D. Truppo, Biocatalysis in the Pharmaceutical Industry: The Need for Speed, ACS Med. Chem. Lett. 8 (2017) 476–480, https://doi.org/10.1021/acsmedchemlett.7b00114.

[4] A. Kinner, P. Nerke, R. Siedentop, T. Steinmetz, T. Classen, K. Rosenthal, M. Nett, J. Pietruszka, S. Lütz, Recent Advances in Biocatalysis for Drug Synthesis, Biomedicines 10 (2022) 964, https://doi.org/10.3390/biomedicines10050964.

[5] M.A. Huffman, A. Fryszkowska, O. Alvizo, M. Borra-Garske, K.R. Campos, K. A. Canada, P.N. Devine, D. Duan, J.H. Forstater, S.T. Grosser, H.M. Halsey, G. J. Hughes, J. Jo, L.A. Joyce, J.N. Kolev, J. Liang, K.M. Maloney, B.F. Mann, N. M. Marshall, M. McLaughlin, J.C. Moore, G.S. Murphy, C.C. Nawrat, J. Nazor, S. Novick, N.R. Patel, A. Rodriguez-Granillo, S.A. Robaire, E.C. Sherer, M. D. Truppo, A.M. Whittaker, D. Verma, L. Xiao, Y. Xu, H. Yang, Design of an in vitro biocatalytic cascade for the manufacture of islatravir, Science 366 (2019) 1255–1259, https://doi.org/10.1126/science.aay8484.

[6] S. Wu, R. Snajdrova, J.C. Moore, K. Baldenius, U.T. Bornscheuer, Biocatalysis: Enzymatic Synthesis for Industrial Applications, Angew. Chem. Int. Ed. 60 (2021) 88–119, https://doi.org/10.1002/anie.202006648.

[7] A. Fryszkowska, P.N. Devine, Biocatalysis in drug discovery and development, Curr. Opin. Chem. Biol. 55 (2020) 151–160, https://doi.org/10.1016/j.cbpa.2020.01.012.

[8] A.S. Bommarius, Biocatalysis: A Status Report, Annu. Rev. Chem. Biomol. Eng. 6 (2015) 319–345, https://doi.org/10.1146/annurev-chembioeng-061114-123415.

[9] J.M. Woodley, Accelerating the implementation of biocatalysis in industry, Appl. Microbiol. Biotechnol. 103 (2019) 4733–4739, https://doi.org/10.1007/s00253-019-09796-x.

[10] R. Barin, D. Biria, S. Rashid-Nadimi, M.A. Asadollahi, Investigating the enzymatic CO_2 reduction to formate with electrochemical NADH regeneration in batch and semi-continuous operations, Chem. Eng. Process. Process Intensif. 140 (2019) 78–84, https://doi.org/10.1016/j.cep.2019.04.020.

[11] S.Z. Çekiç, D. Holtmann, G. Güven, K.-M. Mangold, U. Schwaneberg, J. Schrader, Mediated electron transfer with P450cin, Electrochem. Commun. 12 (2010) 1547–1550, https://doi.org/10.1016/j.elecom.2010.08.030.

[12] H. Zhao, W.A. Van Der Donk, Regeneration of cofactors for use in biocatalysis, Curr. Opin. Biotechnol. 14 (2003) 583–589, https://doi.org/10.1016/j.copbio.2003.09.007.

[13] Y.S. Lee, R. Gerulskis, S.D. Minteer, Advances in electrochemical cofactor regeneration: enzymatic and non-enzymatic approaches, Curr. Opin. Biotechnol. 73 (2022) 14–21, https://doi.org/10.1016/j.copbio.2021.06.013.

[14] R.A. Rincón, C. Lau, K.E. Garcia, P. Atanassov, Flow-through 3D biofuel cell anode for NAD+-dependent enzymes, Electrochim. Acta 56 (2011) 2503–2509, https://doi.org/10.1016/j.electacta.2010.11.041.

[15] C. Cadoux, R.D. Milton, Recent Enzymatic Electrochemistry for Reductive Reactions, ChemElectroChem 7 (2020) 1974–1986, https://doi.org/10.1002/celc.202000282.

[16] K. Délécouls-Servat, R. Basséguy, A. Bergel, Membrane electrochemical reactor (MER): application to NADH regeneration for ADH-catalysed synthesis, Chem. Eng. Sci. 57 (2002) 4633–4642, https://doi.org/10.1016/S0009-2509(02)00393-7.

[17] D. Holtmann, T. Krieg, L. Getrey, J. Schrader, Electroenzymatic process to overcome enzyme instabilities, Catal. Commun. 51 (2014) 82–85, https://doi.org/10.1016/j.catcom.2014.03.033.

[18] A.L. Ghindilis, P. Atanasov, E. Wilkins, Enzyme-catalyzed direct electron transfer: Fundamentals and analytical applications, Electroanalysis 9 (1997) 661–674, https://doi.org/10.1002/elan.1140090902.

[19] F. Harnisch, D. Holtmann (Eds.), Bioelectrosynthesis, Springer International Publishing, Cham, 2019.

[20] S. Arshi, M. Nozari-Asbemarz, E. Magner, Enzymatic Bioreactors: An Electrochemical Perspective, Catalysts 10 (2020) 1232, https://doi.org/10.3390/catal10111232.

[21] M.-C. Fera, K. Jayakumar, D.G. Bueno, J.M. Abad, A.L. De Lacey, M. Pita, Bioelectrocatalytic CO_2 reduction to formate by Candida boidinii formate dehydrogenase overcoming NADH dependence with tailored amino-viologen redox polymers, J. CO_2 Util. 93 (2025) 103041, https://doi.org/10.1016/j.jcou.2025.103041.

[22] K. Jayakumar, M.-C. Fera, J.M. Abad, A.L. De Lacey, M. Pita, Efficient bioelectrocatalytic NADH regeneration with a novel amino-functionalized viologen redox polymer, Bioelectrochemistry 162 (2025) 108850, https://doi.org/10.1016/j.bioelechem.2024.108850.

[23] R. Ullrich, J. Nüske, K. Scheibner, J. Spantzel, M. Hofrichter, Novel haloperoxidase from the agaric basidiomycete *Agrocybe aegerita* oxidizes aryl alcohols and aldehydes, Appl. Environ. Microbiol. 70 (2004) 4575–4581, https://doi.org/10.1128/AEM.70.8.4575-4581.2004.

[24] Y. Cárdenas-Moreno, J. González-Bacerio, H. García Arellano, A. Del Monte-Martínez, Oxidoreductase enzymes: Characteristics, applications, and challenges as a biocatalyst, Biotechnol. Appl. Biochem. 70 (2023) 2108–2135, https://doi.org/10.1002/bab.2513.

[25] A.T. Martínez, F.J. Ruiz-Dueñas, S. Camarero, A. Serrano, D. Linde, H. Lund, J. Vind, M. Tovborg, O.M. Herold-Majumdar, M. Hofrichter, C. Liers, R. Ullrich, K. Scheibner, G. Sannia, A. Piscitelli, C. Pezzella, M.E. Sener, S. Kılıç, W.J.H. Van Berkel, V. Guallar, M.F. Lucas, R. Zuhse, R. Ludwig, F. Hollmann, E. Fernández-Fueyo, E. Record, C.B. Faulds, M. Tortajada, I. Winckelmann, J.-A. Rasmussen, M. Gelo-Pujic, A. Gutiérrez, J.C. Del Río, J. Rencoret, M. Alcalde, Oxidoreductases on their way to industrial biotransformations, Biotechnol. Adv. 35 (2017) 815–831, https://doi.org/10.1016/j.biotechadv.2017.06.003.

[26] M. Hobisch, D. Holtmann, P. Gomez de Santos, M. Alcalde, F. Hollmann, S. Kara, Recent developments in the use of peroxygenases - Exploring their high potential in selective oxyfunctionalisations, Biotechnol. Adv. 51 (2021) 107615, https://doi.org/10.1016/j.biotechadv.2020.107615.

[27] A. Beltrán-Nogal, I. Sánchez-Moreno, D. Méndez-Sánchez, P. Gómez de Santos, F. Hollmann, M. Alcalde, Surfing the wave of oxyfunctionalization chemistry by engineering fungal unspecific peroxygenases, Curr. Opin. Struct. Biol. 73 (2022) 102342, https://doi.org/10.1016/j.sbi.2022.102342.

[28] A.E.W. Horst, S. Bormann, J. Meyer, M. Steinhagen, R. Ludwig, A. Drews, M. Ansorge-Schumacher, D. Holtmann, Electro-enzymatic hydroxylation of ethylbenzene by the evolved unspecific peroxygenase of Agrocybe aegerita, J. Mol. Catal. B Enzym. 133 (2016) 137–142, https://doi.org/10.1016/j.molcatb.2016.12.008.

[29] B.O. Burek, S. Bormann, F. Hollmann, J.Z. Bloh, D. Holtmann, Hydrogen peroxide driven biocatalysis, Green Chem. 21 (2019) 3232–3249, https://doi.org/10.1039/C9GC00633H.

[30] G.V. Sayoga, V.S. Bueschler, H. Beisch, D. Holtmann, A.-P. Zeng, B. Fiedler, D. Ohde, A. Liese, Application of the all-in-one electrode for in situ H_2O_2 generation in hydroxylation catalyzed by unspecific peroxygenase from Agrocybe aegerita, Mol. Catal. 547 (2023) 113325, https://doi.org/10.1016/j.mcat.2023.113325.

[31] S. Bormann, M.M.C.H. van Schie, T.P. Almeida, W. Zhang, M. Stöckl, R. Ulber, F. Hollmann, D. Holtmann, H_2O_2 production at low overpotentials for electroenzymatic halogenation reactions, ChemSusChem 12 (2019) 4759–4763, https://doi.org/10.1002/cssc.201902326.

[32] T. Krieg, A. Sydow, U. Schröder, J. Schrader, D. Holtmann, Reactor concepts for bioelectrochemical syntheses and energy conversion, Trends Biotechnol. 32 (2014) 645–655, https://doi.org/10.1016/j.tibtech.2014.10.004.

[33] A.E.W. Horst, K.-M. Mangold, D. Holtmann, Application of gas diffusion electrodes in bioelectrochemical syntheses and energy conversion, Biotechnol. Bioeng. 113 (2016) 260–267, https://doi.org/10.1002/bit.25698.

[34] M. Stöckl, T. Lange, P. Izadi, S. Bolat, N. Teetz, F. Harnisch, D. Holtmann, Application of gas diffusion electrodes in bioeconomy: An update, Biotechnol. Bioeng. 120 (2023) 1465–1477, https://doi.org/10.1002/bit.28383.

[35] G.V. Sayoga, V.S. Bueschler, H. Beisch, B. Fiedler, D. Ohde, A. Liese, Integration of the All-in-One electrode in an electrochemical flow cell for in situ hydrogen peroxide supply in hydroxylation mediated by immobilized unspecific peroxygenase, Electrochem. Commun. 177 (2025) 107949, https://doi.org/10.1016/j.elecom.2025.107949.

[36] J. Rodrigo Quejigo, S. Tejedor-Sanz, A. Esteve-Núñez, F. Harnisch, Bed electrodes in microbial electrochemistry: setup, operation and characterization, ChemTexts 5 (2019), https://doi.org/10.1007/s40828-019-0078-3.

[37] H. Li, H. Yang, J. Cheng, C. Hu, Z. Yang, C. Wu, Three-dimensional particle electrode system treatment of organic wastewater: A general review based on patents, J. Clean. Prod. 308 (2021) 127324, https://doi.org/10.1016/j.jclepro.2021.127324.

[38] H.L. Wapshott-Stehli, A.M. Grunden, In situ H_2O_2 generation methods in the context of enzyme biocatalysis, Enzym. Microb. Technol. 145 (2021) 109744, https://doi.org/10.1016/j.enzmictec.2021.109744.

[39] S. Bormann, D. Hertweck, S. Schneider, J.Z. Bloh, R. Ulber, A.C. Spiess, D. Holtmann, Modeling and simulation-based design of electroenzymatic batch processes catalyzed by unspecific peroxygenase from A. aegerita, Biotechnol. Bioeng. 118 (2021) 7–16, https://doi.org/10.1002/bit.27545.

[40] G.V. Sayoga, V.S. Bueschler, H. Beisch, T. Utesch, D. Holtmann, B. Fiedler, D. Ohde, A. Liese, Electrochemical H_2O_2 - stat mode as reaction concept to improve the process performance of an unspecific peroxygenase, New Biotechnol. 78 (2023) 95–104, https://doi.org/10.1016/j.nbt.2023.10.007.

[41] G.V. Sayoga, Application of electrochemical approach for in situ H_2O_2 generation in enzyme catalysis, Technical University of Hamburg, 2025. https://tore.tuhh.de/handle/11420/57981 (accessed January 24, 2026).

[42] R. Zou, A. Hasanzadeh, A. Khataee, X. Yang, M. Xu, I. Angelidaki, Y. Zhang, Scaling-up of microbial electrosynthesis with multiple electrodes for in situ production of hydrogen peroxide, iScience 24 (2021) 102094, https://doi.org/10.1016/j.isci.2021.102094.

[43] Y. Lu, G. Liu, H. Luo, R. Zhang, Efficient in-situ production of hydrogen peroxide using a novel stacked electrosynthesis reactor, Electrochim. Acta 248 (2017) 29–36, https://doi.org/10.1016/j.electacta.2017.07.085.
[44] A. Tschöpe, M. Wyrwoll, M. Schneider, K. Mandel, M. Franzreb, A magnetically induced fluidized-bed reactor for intensification of electrochemical reactions, Chem. Eng. J. 385 (2020) 123845, https://doi.org/10.1016/j.cej.2019.123845.
[45] A. Tschöpe, S. Heikenwälder, M. Schneider, K. Mandel, M. Franzreb, Electrical conductivity of magnetically stabilized fluidized-bed electrodes – Chronoamperometric and impedance studies, Chem. Eng. J. 396 (2020) 125326, https://doi.org/10.1016/j.cej.2020.125326.
[46] A. Tschöpe, M. Franzreb, Influence of non-conducting suspended solids onto the efficiency of electrochemical reactors using fluidized bed electrodes, Chem. Eng. J. 424 (2021) 130322, https://doi.org/10.1016/j.cej.2021.130322.
[47] M. Klaiber, A. Tschöpe, K. Cu, I. Waibel, S. Heißler, M. Franzreb, J. Lahann, Multifunctional core–shell particle electrodes for application in fluidized bed reactors, ACS Appl. Eng. Mater. 1 (2023) 325–333, https://doi.org/10.1021/acsaenm.2c00072.
[48] M. Schneider, A. Tschöpe, D. Hanselmann, T. Ballweg, C. Gellermann, M. Franzreb, K. Mandel, Adsorber Particles with Magnetically-Supported Improved Electrochemical Conversion Behavior for Waste Water Treatment Processes, Part. Part. Syst. Charact. 37 (2020) 1900487, https://doi.org/10.1002/ppsc.201900487.
[49] B. Korth, N. Pous, R. Hönig, P. Haus, F.B. Corrêa, U. Nunes Da Rocha, S. Puig, F. Harnisch, Electrochemical and Microbial Dissection of Electrified Biotrickling Filters, Front. Microbiol. 13 (2022) 869474, https://doi.org/10.3389/fmicb.2022.869474.
[50] A. Ceballos-Escalera, N. Pous, B. Korth, F. Harnisch, M.D. Balaguer, S. Puig, Ex-situ electrochemical characterisation of fixed-bed denitrification biocathodes: A promising strategy to improve bioelectrochemical denitrification, Chemosphere 347 (2024) 140699, https://doi.org/10.1016/j.chemosphere.2023.140699.
[51] M. Abt, M. Franzreb, M. Jestädt, A. Tschöpe, Three-phase fluidized bed electrochemical reactor for the scalable generation of hydrogen peroxide at enzyme compatible conditions, Chem. Eng. J. 476 (2023) 146465, https://doi.org/10.1016/j.cej.2023.146465.
[52] J.R. Quejigo, B. Korth, A. Kuchenbuch, F. Harnisch, Redox Potential Heterogeneity in Fixed-Bed Electrodes Leads to Microbial Stratification and Inhomogeneous Performance, ChemSusChem 14 (2021) 1155–1165, https://doi.org/10.1002/cssc.202002611.
[53] S. Lütz, K. Vuorilehto, A. Liese, Process development for the electroenzymatic synthesis of (R)-methylphenylsulfoxide by use of a 3-dimensional electrode, Biotechnol. Bioeng. 98 (2007) 525–534, https://doi.org/10.1002/bit.21434.
[54] K. Vuorilehto, S. Lütz, C. Wandrey, Indirect electrochemical reduction of nicotinamide coenzymes, Bioelectrochemistry 65 (2004) 1–7, https://doi.org/10.1016/j.bioelechem.2004.05.006.
[55] S. Kochius, J.B. Park, C. Ley, P. Könst, F. Hollmann, J. Schrader, D. Holtmann, Electrochemical regeneration of oxidised nicotinamide cofactors in a scalable reactor, J. Mol. Catal. B Enzym. 103 (2014) 94–99, https://doi.org/10.1016/j.molcatb.2013.07.006.
[56] Y. Asensio, M. Llorente, P. Fernández, S. Tejedor-Sanz, J.M. Ortiz, J.F. Ciriza, V. Monsalvo, F. Rogalla, A. Esteve-Núñez, Upgrading fluidized bed bioelectrochemical reactors for treating brewery wastewater by using a fluid-like electrode, Chem. Eng. J. 406 (2021) 127103, https://doi.org/10.1016/j.cej.2020.127103.
[57] Y. Asensio, M. Llorente, A. Sánchez-Gómez, C. Manchon, K. Boltes, A. Esteve-Núñez, Microbial Electrochemical Fluidized Bed Reactor: A Promising Solution for Removing Pollutants From Pharmaceutical Industrial Wastewater, Front. Microbiol. 12 (2021) 737112, https://doi.org/10.3389/fmicb.2021.737112.
[58] S. Tejedor-Sanz, J.M. Ortiz, A. Esteve-Núñez, Merging microbial electrochemical systems with electrocoagulation pretreatment for achieving a complete treatment of brewery wastewater, Chem. Eng. J. 330 (2017) 1068–1074, https://doi.org/10.1016/j.cej.2017.08.049.
[59] P. Molina-Espeja, E. Garcia-Ruiz, D. Gonzalez-Perez, R. Ullrich, M. Hofrichter, M. Alcalde, Directed evolution of unspecific peroxygenase from Agrocybe aegerita, Appl. Environ. Microbiol. 80 (2014) 3496–3507, https://doi.org/10.1128/AEM.00490-14.
[60] P. Molina-Espeja, S. Ma, D.M. Mate, R. Ludwig, M. Alcalde, Tandem-yeast expression system for engineering and producing unspecific peroxygenase, Enzym. Microb. Technol. 73–74 (2015) 29–33, https://doi.org/10.1016/j.enzmictec.2015.03.004.
[61] F. Tonin, F. Tieves, S. Willot, A. van Troost, R. van Oosten, S. Breestraat, S. van Pelt, M. Alcalde, F. Hollmann, Pilot-Scale Production of Peroxygenase from Agrocybe aegerita, Org. Process. Res. Dev. 25 (2021) 1414–1418, https://doi.org/10.1021/acs.oprd.1c00116.
[62] G. Sayoga, M. Abt, N. Teetz, V. Bueschler, A. Liese, M. Franzreb, D. Holtmann, Quantitative and Non-Quantitative Assessments of Enzymatic Electrosynthesis: A Case Study of Parameter Requirements, ChemElectroChem (2023), https://doi.org/10.1002/celc.202300226.
[63] Y. Pang, H. Xie, Y. Sun, M.-M. Titirici, G.-L. Chai, Electrochemical oxygen reduction for H_2O_2 production: catalysts, pH effects and mechanisms, J. Mater. Chem. A 8 (2020) 24996–25016, https://doi.org/10.1039/D0TA09122G.
[64] R. Mireles, J. Ramirez-Ramirez, M. Alcalde, M. Ayala, Ether oxidation by an evolved fungal heme-peroxygenase: insights into substrate recognition and reactivity, J. Fungi 7 (2021), https://doi.org/10.3390/jof7080608.
[65] S. Peter, A. Karich, R. Ullrich, G. Gröbe, K. Scheibner, M. Hofrichter, Enzymatic one-pot conversion of cyclohexane into cyclohexanone: Comparison of four fungal peroxygenases, J. Mol. Catal. B Enzym. 103 (2014) 47–51, https://doi.org/10.1016/j.molcatb.2013.09.016.
[66] A. Karich, K. Scheibner, R. Ullrich, M. Hofrichter, Exploring the catalase activity of unspecific peroxygenases and the mechanism of peroxide-dependent heme destruction, J. Mol. Catal. B Enzym. 134 (2016) 238–246, https://doi.org/10.1016/j.molcatb.2016.10.014.
[67] S. Last, T. Heinks, N. Dietz, S. Koopmeiners, G. Fischer Von Mollard, M. J. Weissenborn, J. Von Langermann, Constant enzymatic in situ production of H_2O_2 for an unspecific peroxygenase by an l– amino acid oxidase, Adv. Synth. Catal. 367 (2025) e202500105, https://doi.org/10.1002/adsc.202500105.
[68] S. Bormann, B.O. Burek, R. Ulber, D. Holtmann, Immobilization of unspecific peroxygenase expressed in Pichia pastoris by metal affinity binding, Mol. Catal. 492 (2020) 110999, https://doi.org/10.1016/j.mcat.2020.110999.
[69] S.C. Perry, D. Pangotra, L. Vieira, L.-I. Csepei, V. Sieber, L. Wang, C. Ponce de León, F.C. Walsh, Electrochemical synthesis of hydrogen peroxide from water and oxygen, Nat. Rev. Chem. 3 (2019) 442–458, https://doi.org/10.1038/s41570-019-0110-6.
[70] A. Da Pozzo, L. Di Palma, C. Merli, E. Petrucci, An experimental comparison of a graphite electrode and a gas diffusion electrode for the cathodic production of hydrogen peroxide, J. Appl. Electrochem. 35 (2005) 413–419, https://doi.org/10.1007/s10800-005-0800-2.